Icarus 311 (2018) 317–339

Contents lists available at ScienceDirect

Icarus

journal homepage: www.elsevier.com/locate/icarus

Vertical wind shear in Neptune's upper atmosphere explained with a modified thermal wind equation

Joshua Tollefson[a,*], Imke de Pater[a,b], Philip S. Marcus[c], Statia Luszcz-Cook[d], Lawrence A. Sromovsky[e], Patrick M. Fry[e], Leigh N. Fletcher[f], Michael H. Wong[b]

[a] Department of Earth and Planetary Science, University of California, Berkeley, CA 94720, USA
[b] Department of Astronomy, University of California, Berkeley, CA 94720, USA
[c] Department of Mechanical Engineering, University of California, Berkeley, CA 94720, USA
[d] Department of Astrophysics, American Museum of Natural History, 79th Street at Central Park West, New York, NY 10024, USA
[e] Space Science and Engineering Center, University of Wisconsin, Madison, WI 53706, USA
[f] Department of Physics and Astronomy, University of Leicester, University Road, Leicester LE1 7RH, UK

ARTICLE INFO

Article history:
Received 20 May 2016
Revised 27 March 2018
Accepted 11 April 2018
Available online 19 April 2018

ABSTRACT

We present observations of Neptune taken in H-(1.4–1.8 μm) and K'-(2.0–2.4 μm) bands on the nights of July 3, 2013 and August 20, 2014 from the 10-m W.M. Keck II Telescope using NIRC2 coupled to the Adaptive Optics (AO) system. We track the positions of ~100 bright atmospheric features over a 4–5 h window on each night to derive zonal velocities and wind profiles.

Our results deviate from the smooth Voyager zonal wind profile from Sromovsky et al. (1993), often by 100–200 m/s, and often by 3–10 times their estimated uncertainties. Besides what appears to be a random dispersion, probably due to a mix of unaccounted for measurement errors, eddy motions, vertical wind shear, and wave-generated features that do not follow the mass flow, there is also a systematic deviation that is wavelength dependent. The H-band profile is best described with a 73–106 m/s shift towards the east for a retrograde flow (i.e., a lessening of the retrograding velocities) from the Voyager profile at the equator. The K'-band profile is consistent with Voyager on both nights.

Comparing H and K' contribution functions and K'/H intensities suggests equatorial H-band features are, on average, deeper than K'-band features. The H-band equatorial features also have greater eastward (less negative) velocities than K'-band features. Differences in zonal wind speed with depth at constant latitude and time imply vertical wind shear. Assuming the average variations in the zonal wind profiles result from wind shear over 3–5 scale heights, we predict vertical wind shears between −1.0 and −2.2 m/(s km) at the equator (increasing with height).

The standard thermal wind equation and meridional thermal profile for Neptune given by Voyager/IRIS spectra predict wind shear of the wrong sign relative to the observations. We consider two effects that reconcile this inconsistency. First, we calculate the meridional temperature gradients at pressures outside the Voyager/IRIS narrow sensitivity window required to match our predicted wind shears. Second, we generalize to a thermal wind equation that considers global methane variations and re-derive the temperature structure needed to match the observed wind shear. If methane is uniformly distributed or weakly varying, the equator must be 2–15 K cooler than the mid latitudes below 1 bar. If methane is strongly varying, the equator can be 2–3 K warmer than the mid latitudes below 1 bar, qualitatively consistent with observed temperature contrasts. These findings may imply a stacked-celled circulation pattern in Neptune's troposphere and lower stratosphere.

1. Introduction

The zonal wind velocities of the giant planets are obtained by tracking bright cloud features in their atmospheres. Sromovsky et al. (1993) created a zonal wind profile for Neptune by

* Corresponding author.
E-mail address: jtollefs@berkeley.edu (J. Tollefson).

https://doi.org/10.1016/j.icarus.2018.04.009
0019-1035/

constructing a fit to measurements of position and velocity of discrete cloud features by Limaye and Sromovsky (1991) from Voyager 2 images taken in visible wavelengths. Derived velocities were averaged in latitudinal bins and fit to a fourth-order polynomial to create a smooth zonal wind profile, also referred to as the canonical profile. This profile revealed Neptune's atmospheric winds are extremely strong, despite Neptune receiving minimal solar insolation. Equatorial wind speeds reach up to 400 m/s, some of the fastest in the solar system.

Cloud tracking studies have shown significant deviations from Neptune's canonical wind profile. Limaye and Sromovsky (1991) saw deviations on the order of 50 m/s, particularly in clouds around the vicinity of a Great Dark Spot (GDS) and at Northern latitudes between 25°–30° N. Sromovsky et al. (1993) found dispersion in cloud velocities from their constructed canonical profile. Hammel and Lockwood (1997) also saw dispersion of velocities in narrow latitude strips from 1995 HST maps. Sromovsky et al. (2001b,c) tracked features in 1996 data and found general agreement with the canonical profile apart from features close to a dark spot. These findings suggest Neptune's clouds are not all passive tracers for the background winds, but may also be evidence of wind shear, wave propagation from the presence of vortices, such as the GDS, or other local phenomena.

Recent fits to the zonal wind profile using near-infrared imaging data show shifts relative to the canonical profile, in addition to the dispersion of clouds at a given latitude noted by earlier studies. Fitzpatrick et al. (2014) tracked dozens of bright atmospheric features using Keck AO images in the H-band and found that a profile with a ~180 m/s eastward shift from the canonical profile at the equator best matched the data. Martin et al. (2012) also observed many cloud features in the H-band (1.6 μm) that appeared to not move with the canonical profile, with differences reaching as large as 500 m/s. Interestingly, Fitzpatrick et al. (2014) also tracked features in K'-band (2.2 μm) images and found that the derived profile was consistent with the Voyager profile. They suggested that the eastward shift in the H-band profile from the K'-band and Voyager profiles could be due to temporal changes or a wavelength/depth effect.

However, the exact mechanisms that drive the dispersion and profile shifts in the zonal winds of Neptune remain largely unresolved. Martin et al. (2012) observed wave-like behavior in the east-west motions of several cloud features with periods close to the 7.2 h period of the principal semi-diurnal tides from Triton. They suggested that future observations look at the effect of tidal forcing from Triton on the velocities of Neptune's cloud features. Recent *Kepler* observations did not find signals in photometric light curves corresponding to the periods of Neptune's major moons, disproving this idea (Simon et al., 2016). Fitzpatrick et al. (2014) used radiative transfer models to determine the approximate altitudes of clouds and concluded that the differences between their observed wind profiles in H- and K'-bands were too large in magnitude and in the opposite direction than what could be explained by vertical wind shear. Evidence of large north-south velocities in feature motions may be due to vortices or various wave mechanisms but the exact cause of zonal wind variability is unknown.

A major drawback to the studies conducted by Martin et al. (2012) and Fitzpatrick et al. (2014) is that they either: imaged at one wavelength, so that differences in wind speed versus atmospheric depth cannot be seen; or performed cloud tracking at two wavelengths on different nights so that the two cannot be directly compared. With these issues in mind, we perform analyses similar to Martin et al. (2012) and Fitzpatrick et al. (2014) to test the vertical wind shear hypothesis for zonal wind dispersion on Neptune. We first present observations of Neptune taken in the H-(1.4–1.8 μm) and K'-(2.0–2.4 μm) bands on each of the nights of July 3, 2013 and August 20, 2014 and derive zonal wind profiles for each band by tracking the motions of bright cloud features. We remark on observed differences between the H- and K'-band profiles in the equatorial region, leading us to reconsider vertical wind shear as being important, as we observe differences in speeds for features at the same latitudes and time. We then discuss the applicability of the thermal wind equation to model vertical wind shear in Neptune's troposphere and lower stratosphere from the equator to mid-latitudes. Finally, we examine the physical consequences of vertical wind shear in terms of Neptune's global circulation.

2. Data

2.1. Observations and data reduction

We observed Neptune's atmosphere on July 3, 2013 and August 20, 2014 UT from the Keck II Telescope on Mauna Kea, Hawaii at Near-Infrared (NIR) wavelengths. H- (1.4–1.8 μm) and K'- (2.0–2.4 μm) band images were taken on both nights with the narrow camera of the NIRC2 instrument coupled to the Adaptive Optics (AO) system. The detector is a 1024 × 1024 array with a scale of 0.009942 arcsec/pixel in this view (de Pater et al., 2006).

A total of 75 images were taken in each band on July 3, 2013 from 10:48–15:09 (UT); 100 images were taken in each band on August 20, 2014 from 08:13–13:30 (UT). An integration time of 60 seconds was used for all images. This provides the best compromise of high signal to noise while minimizing feature smearing and avoiding over-saturating the detector. Moreover, short integration times allow many images to be taken over the observation period and ensure the identification of the same features in successive images. Images were taken in sets of five and alternated between the H- and K'-bands, corresponding to a ~15 min separation between image sets in a single band.

Images were reduced using standard infrared reduction techniques of sky subtraction, flat fielding, and median-value masking to remove bad pixels. We estimate <1% of the total number of pixels are bad, more than half of which are confined to one quadrant of the detector. Care was taken to image Neptune away from this quadrant. Each image was corrected for the geometric distortion of the array using the 'dewarp' routines provided by Brian Cameron,[1] who estimates residual errors at ≤0.1 pixels.

We photometrically calibrated images using the Elias standard stars (Elias et al., 1982) HD162208 on July 3, 2013 and HD1160 on August 20, 2014 and converted them to units of I/F, defined as (Hammel et al., 1989):

$$\frac{I}{F} = \frac{r^2}{\Omega}\frac{F_N}{F_\odot} \tag{1}$$

Here, r is the ratio of Neptune's to Earth's heliocentric distance in A.U., $\pi F_\odot$ is the Sun's flux density at Earth's orbit, F_N is Neptune's observed flux density, and Ω is the solid angle subtended by a pixel on the detector.

2.2. Imaging results

Fig. 1 shows calibrated images of Neptune at the beginning and end of each observing night and in each band. Because there were problems in the optical alignment of the AO system on the night of August 20, 2014, we did not achieve expected (diffraction-limited) resolution. This resulted in limited feature tracking capabilities for these images. Our viewing is limited to latitudes south of +50° due to the sub-Earth latitude of −27°.

[1] http://www2.keck.hawaii.edu/inst/nirc2/forReDoc/postobserving/dewarp/nirc2dewarp.pro.

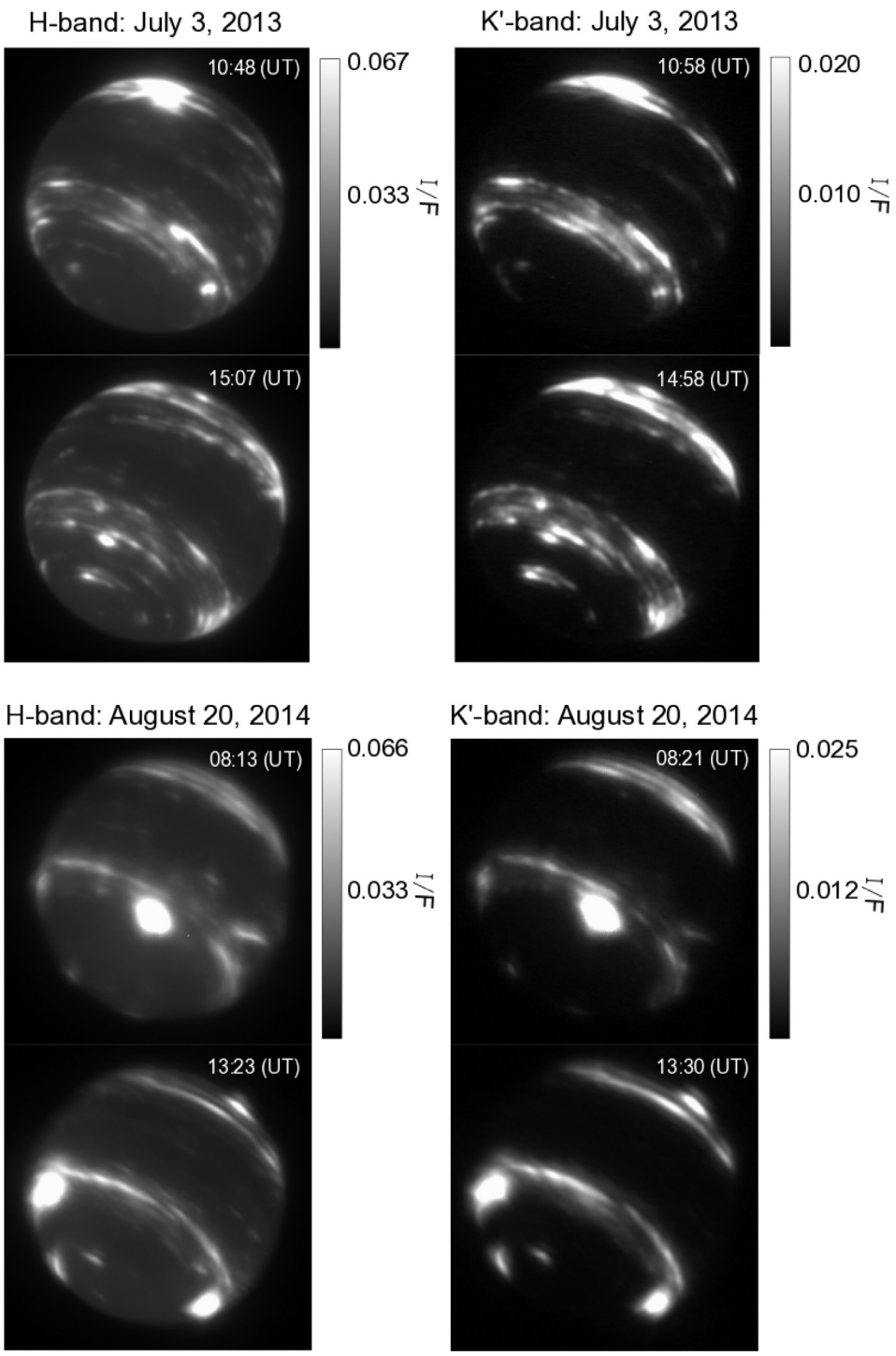

Fig. 1. Images of Neptune taken in the H-(left columns) and K'-(right columns) taken on July 3, 2013 (top) and August 20, 2014 (bottom). The first and last images taken of Neptune on a given night are shown for each band. Images are in units of I/F with a colorbar given on the right of each image set.

Cloud features can be seen in both bands on both nights and their general characteristics agree with previous observations (e.g. Sromovsky et al., 2001a; Max et al., 2003; Martin et al., 2012; Fitzpatrick et al., 2014). The brightest clouds stretch along several constant latitude bands centered at the mid-latitudes. On July 3, 2013, we see the largest bright feature centered at about 40°N. By August 20, 2014, this feature had disappeared or migrated to the dark side of the planet. Instead, we see two bright features in the Southern hemisphere centered at roughly 40°S. In the H-band, we also see a feature at Neptune's south pole, seen since the Voyager era (e.g. Smith et al., 1989; Limaye and Sromovsky, 1991; Luszcz-Cook et al., 2010; Fitzpatrick et al., 2014; de Pater et al., 2014). No features are seen immediately south of the equator.

Fig. 2(a) and (c) shows single images of Neptune that have been produced by combining the set of July 3, 2013 H- and K'-band images, respectively, using a procedure described in Fry et al. (2012). The image combination increases the S/N ratio of the images by employing a pixel brightness averaging method and correcting for feature motions induced by rotation and the canonical zonal wind profile. We did not make such images for August 20,

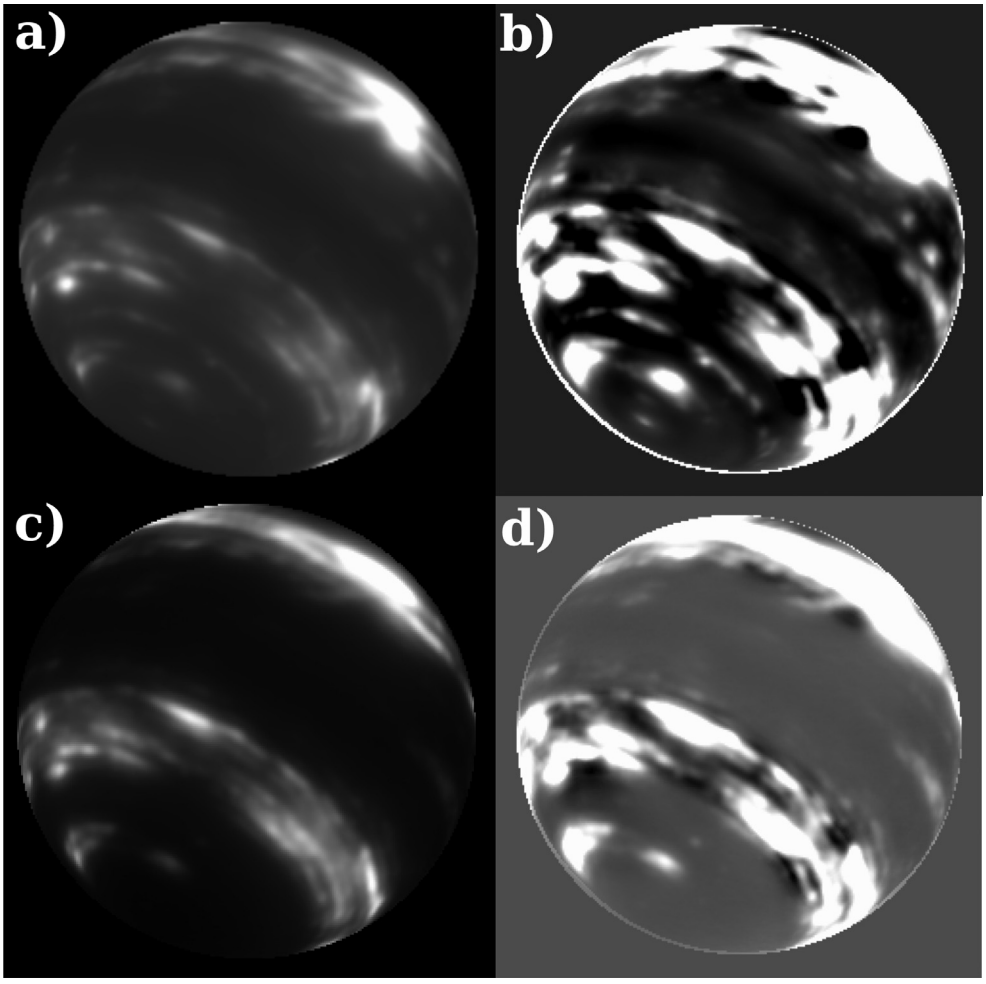

Fig. 2. Images of Neptune in the H-band (top row) and K'-band (bottom row) on July 3, 2013 using the image combination method described in Fry et al. (2012). Figs. (a) and (c) show the unaltered image while (b) and (d) show an enhanced, high-pass filtered version. Subtle equatorial features and banding can be made out due to the increased S/N ratio.

2014 due to the poor AO performance. In Fig. 2, (b) and (d) are (a) and (c) passed through a high-pass filter by subtracting a median-smoothed image. Banding at the equator can be made out as well as several subtle features. More features can be identified around the equator in the H-band compared to the K'-band.

2.3. Image navigation and projection

Accurate navigation and feature tracking requires precise determinations of Neptune's center in each image. An offset of even one pixel in the image centering can dramatically alter an image's projection and the determination of feature locations. This is seen in Fig. 4 of Martin et al. (2012), which shows the errors due to a shift in the center of the disk in a map projection. We derive image centers by fitting the observed positions of three moons to their orbits as generated by the Rings Node of NASA's Planetary Data System (http://pds-rings.seti.org/) with a χ^2 minimization routine using a method developed by Luszcz-Cook et al. (2010) and used by Fitzpatrick et al. (2014). The error in image center was estimated by the variance in observed orbit to modeled orbit modified by a factor of the reduced χ^2. The estimated mean uncertainty of the center in both the H- and K'-band images on each night is between 0.1 and 0.2 pixels in x and y coordinates.

The accuracy of this procedure can be judged in Fig. 3. Shown are the mean images of the aligned image stacks in each band on July 3, 2013. Each averaged image was passed through a high-pass filter by subtracting a median-smoothed image. This allows the individual orbits of Despina, Galatea, and Larissa to be resolved. Overlain on each image are the Rings Node moon orbits, which align well with the observed orbits after image alignment and navigation.

Images are then projected onto a rectangular grid and averaged over the five frames within each image set, with the rotation rate of the planet removed (about 16.11 h, or 1.86°/5 min). Generally, the zonal drift rates are smaller (<0.65°/5 min) than the angular resolution at disk center (~2.4°). Hence, averaging images does not significantly smear features, but increases the signal-to-noise and allows fainter features to be distinguished. Averaging sets of data yielded 15 images in both bands on July 3, 2013 and 20 images in both bands on August 20, 2014.

3. Atmospheric feature tracking

The velocities of cloud features act as tracers for atmospheric wind velocities. Fig. 4 is a rectangular projection of Fig. 2(a) and (c) and shows candidate features identified for tracking. Features which are bright and morphologically stable over ~1 h are candidates for tracking. Moreover, a feature must be distinct in longitude and latitude to be considered for tracking. In both bands, trackable features are most common at the mid-latitudes. Near the equator, both bands are relatively dark, with slightly more trackable features in H-band compared to K'-band.

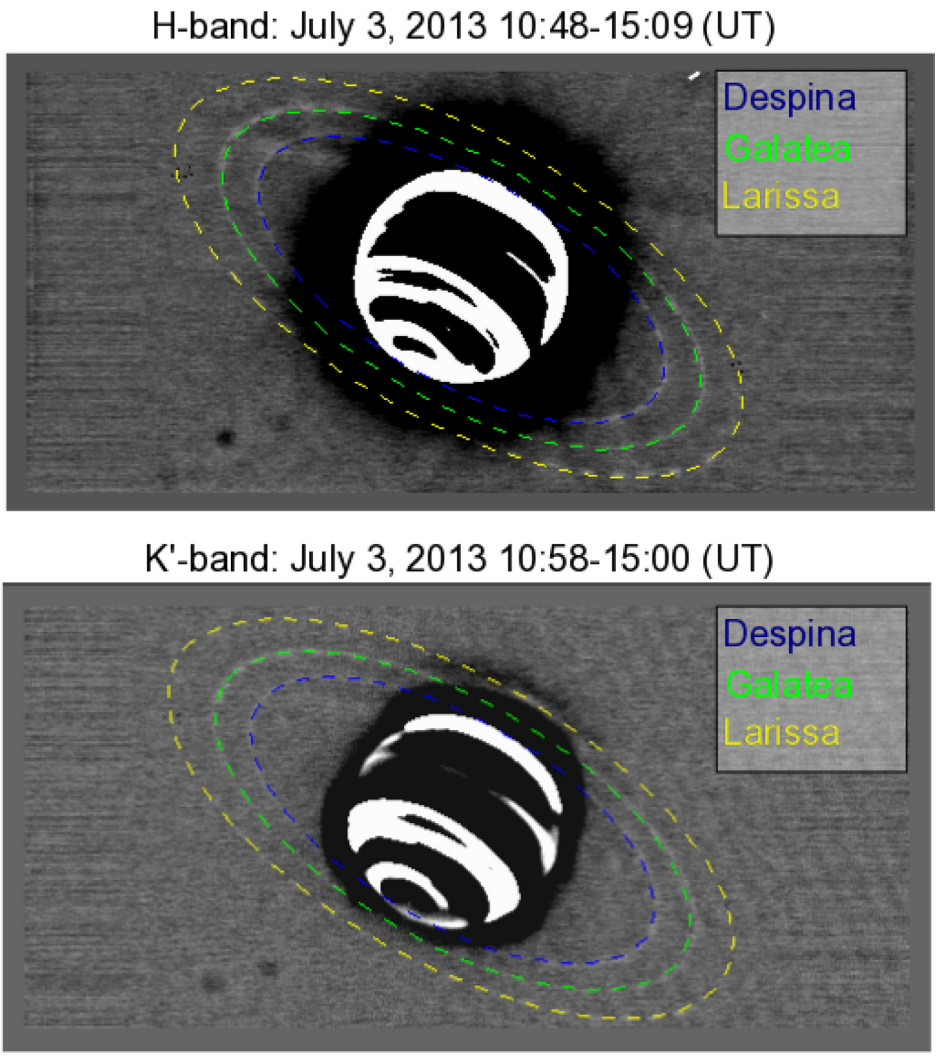

Fig. 3. Mean averaged, high-pass filtered images of the aligned image stacks taken on July 3, 2013 in the H-(top) and K'-(bottom) bands. The colored dashed lines are the Ring Nodes orbits of three Neptunian moons (Despina, Galatea, and Larissa) and were used to determine the center of Neptune for navigation purposes. The path of each moon is seen as faint gray ellipses in these combined image stacks. The NASA orbits overlay the moon positions in the aligned images nicely, suggesting adequate navigation.

The procedure for extracting wind velocities from feature positions is described in detail in Sromovsky et al. (2012). To summarize, from the projected, averaged images we produce strips of images in a fixed latitude range stacked in a vertical time series. An example of this image stack is given in Fig. 5. For each visible feature, a reference image is chosen and centered around a target box containing the feature and a region outside it. Target boxes are placed in all other image strips based on the Voyager canonical longitudinal drift rates for Neptune and their positions are adjusted to maximize the cross-correlation between the feature signals in the reference target box and those in the other images. The centers of each box are the predicted longitude and latitude of the feature in each image. Fig. 6 gives an example output of this method, which plots the predicted centers and correlation for each time slice of one feature.

Measured longitudes and latitudes vs. time were fit to straight lines with weighted regressions. Errors in position are given as the RMS deviation from a straight line. We repeat this procedure for dozens of features. In Figs. 7 and 8, we plot the longitude position of selected tracked features versus time. Plots for all features can be found in Supplementary Materials 2. While most features, within their estimated error, follow the drift rates expected by the canonical profile, many deviate significantly. Differences from the anticipated drift rate could be real or due to measurement errors and will be further discussed in later sections. Tables 1–4 in Supplementary Materials 1 summarize all tracked feature information.

4. Results

4.1. Zonal wind profiles

Longitudinal and latitudinal drift rates are transformed into zonal and meridional velocities by the following equations for planetocentric latitudes (Sromovsky et al., 2001b):

$$V_{\text{lon}} = \frac{R_{\text{eq}}}{\sqrt{1 + \frac{R_{\text{eq}}^2}{R_{\text{pol}}^2}\tan^2\theta}}\frac{d\phi}{dt} \tag{2}$$

$$V_{\text{lat}} = \frac{R_{\text{pol}}^2}{R_{\text{eq}}}\left(\frac{1 + \frac{R_{\text{eq}}^4}{R_{\text{pol}}^4}\tan^2\theta}{1 + \frac{R_{\text{eq}}^2}{R_{\text{pol}}^2}\tan^2\theta}\right)^{\frac{3}{2}}\frac{d\theta}{dt} \tag{3}$$

Here, V is the wind speed in m/s, R_{eq} and R_{pol} are the equatorial and polar radii of Neptune, equal to 2.4766×10^7 m and 2.4342×10^7 m respectively (Lindal, 1992). $d\theta/dt$ and $d\phi/dt$ are the derived zonal and meridional drift rates (rad/s). Velocities for

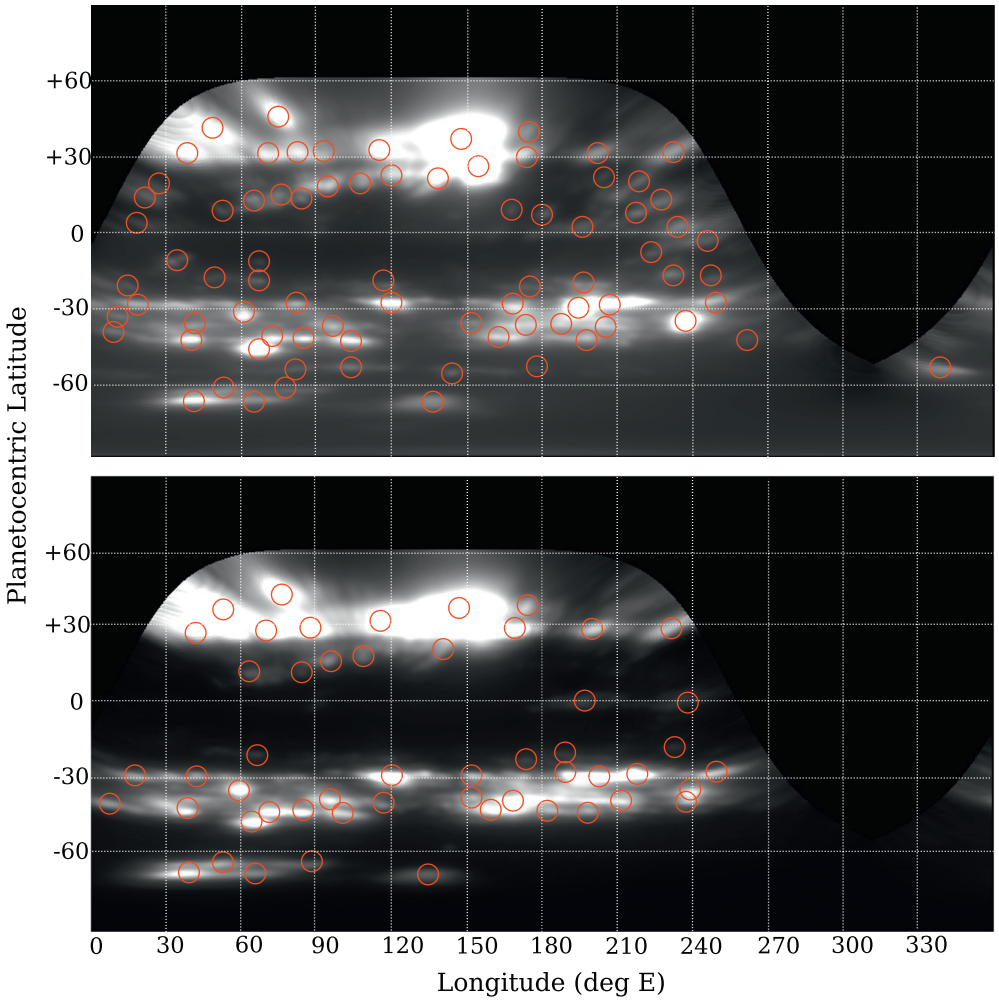

Fig. 4. Rectangular projections of Fig. 2(a) (H-band; top) and (c) (K'-band; bottom). Red circles are potential trackable features.

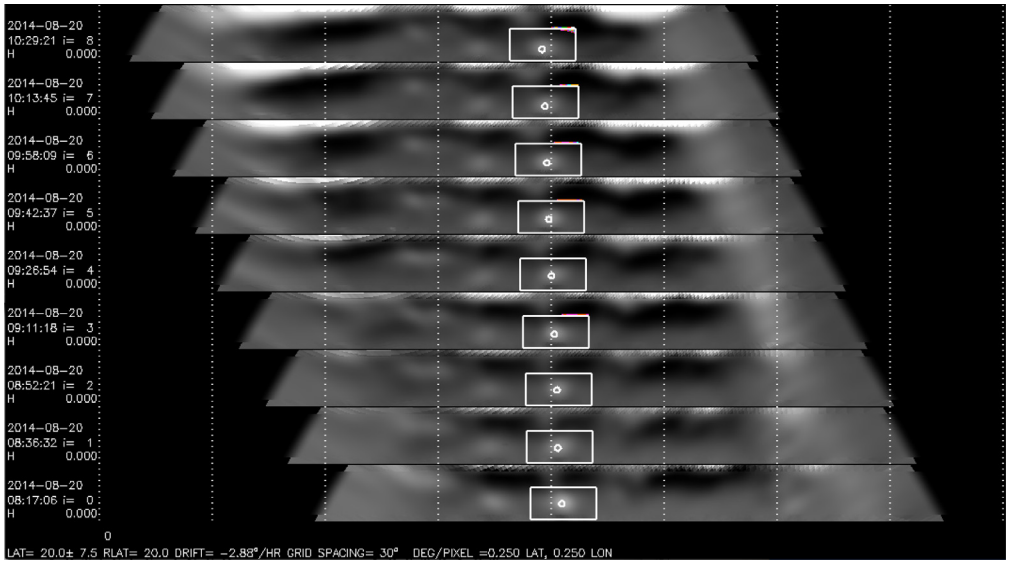

Fig. 5. Example deprojected image strips at a fixed latitude range (20° ± 7.5°N) stacked vertically by time since the initial observation. Each image strip is an average of a set of five images. Vertical white lines mark 30° increments in longitude. An example target feature of the tracking method is outlined in each box and its center is the result of maximizing the cross-correlation between image sets.

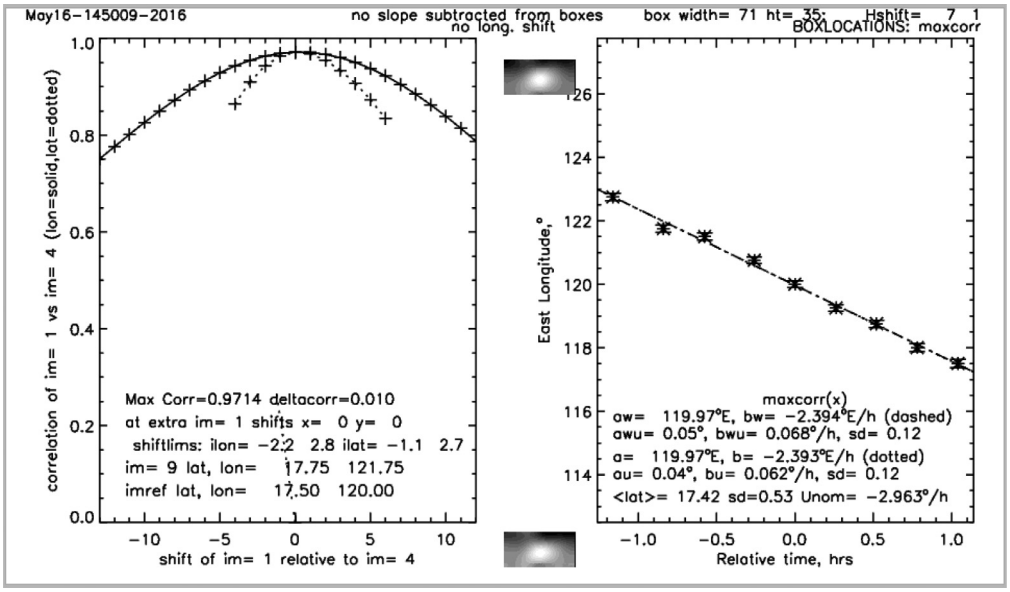

Fig. 6. The output of the feature tracking method showing the predicted longitude positions (right) from maximizing the cross-correlation between image slices (left) for one particular feature (see Fig. 5). Left: the solid lines are the correlation between longitudinal positions and the dashed lines are the correlation between latitudinal positions. Right: the black dots are the predicted longitude based on maximizing the correlation between image slices. The dash–dot line is a line of best fit through the black (correlation) points. The selected feature at the initial and end frames is shown in the center.

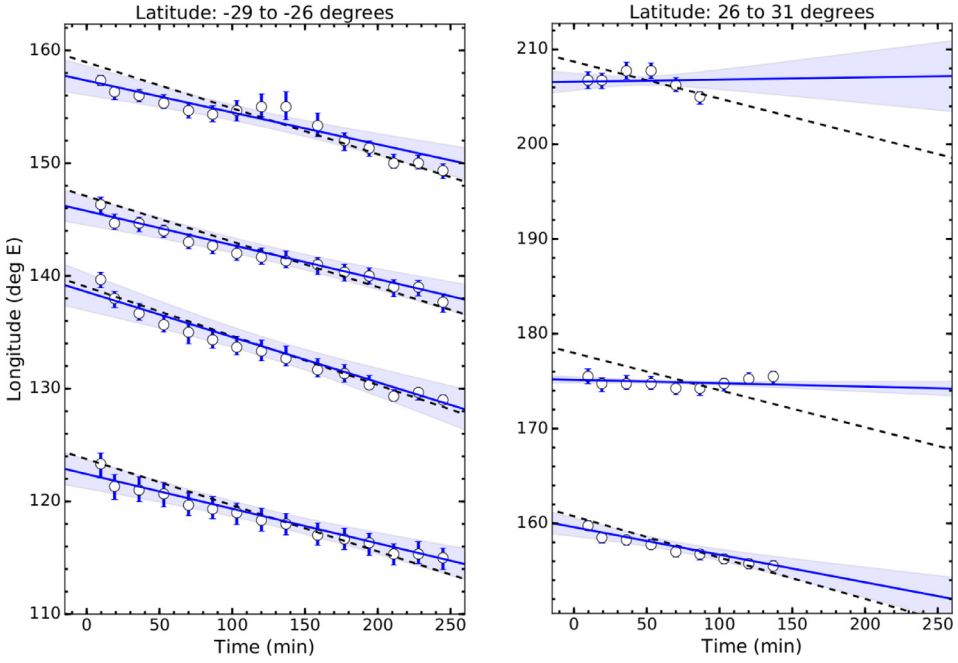

Fig. 7. Selected feature tracking results in the H-band from July 3, 2013. Each data point is a feature's derived longitude since the initial observation. The blue lines are lines of best fit to the data. The blue shaded region is the 1σ error in the fit. The dashed black line is the longitude path the feature would follow according to the canonical profile. The majority of tracked features follow the canonical profile (left figure), but some deviate significantly (right figure). Plots for all features can be found in Supplementary Materials 2. (For interpretation of the references to color in this figure legend, the reader is referred to the web version of this article.)

each feature are then plotted as a function of latitude and fit to a fourth-order polynomial symmetric about the equator. Neptune rotates from west to east, in the same direction as Earth, and eastward winds are taken to be positive. Thus the equatorial winds on Neptune are retrograde, blowing opposite to the direction of the planet's rotation, unlike Jupiter and Saturn, where equatorial winds are eastward and prograde. Comparisons to our profiles in both bands and the canonical profile are shown in Figs. 9 and 10. Table 1 lists the parameters of each fitted polynomial and their widths of uncertainty.

A significant, large spread in the individual derived zonal velocities is observed at constant latitudes on both nights. This is most prominent at the equator and mid-latitudes in both bands, with differences in feature velocities reaching as high as 500–600 m/s. Moreover, there is a pronounced difference between the derived H and K' zonal wind profiles near the equator. At the equator on July 3, 2013, the deviation in the H-band wind speeds compared to those derived by the Voyager fit is 73 ± 16 m/s. The difference between the H- and K'-bands on this night at the equator is 90 ± 45 m/s. This shift persists in the August 20, 2014 observa-

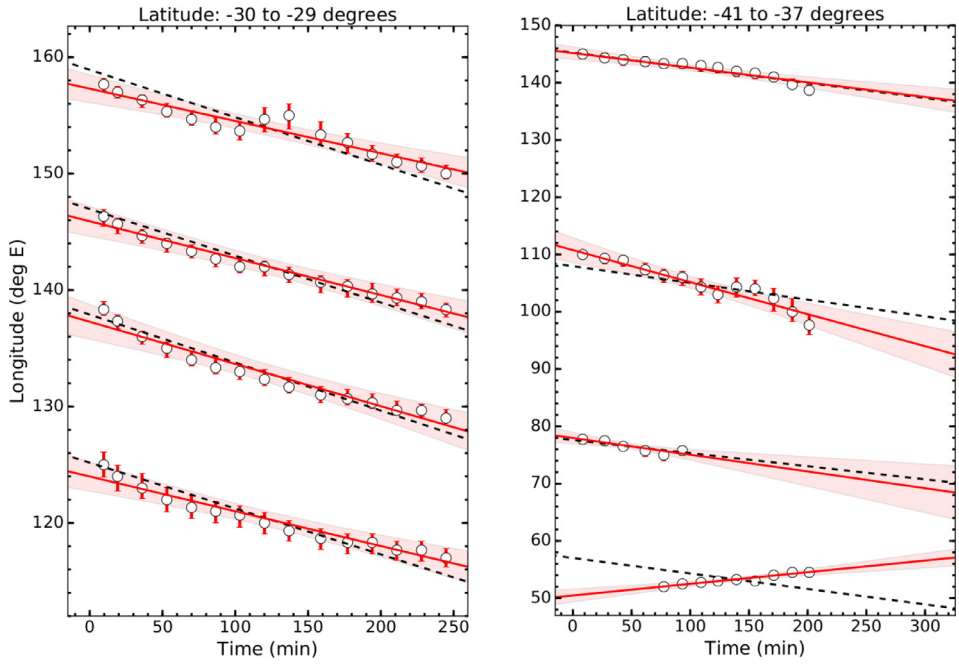

Fig. 8. As Fig. 5 except for the K'-band. The red lines are lines of best fit to the data. The red shaded region is the 1σ error in the fit. The dashed black line is the longitude path the feature would follow according to the canonical profile. The majority of tracked features follow the canonical profile (left figure), but some deviate significantly (right figure). (For interpretation of the references to color in this figure legend, the reader is referred to the web version of this article.)

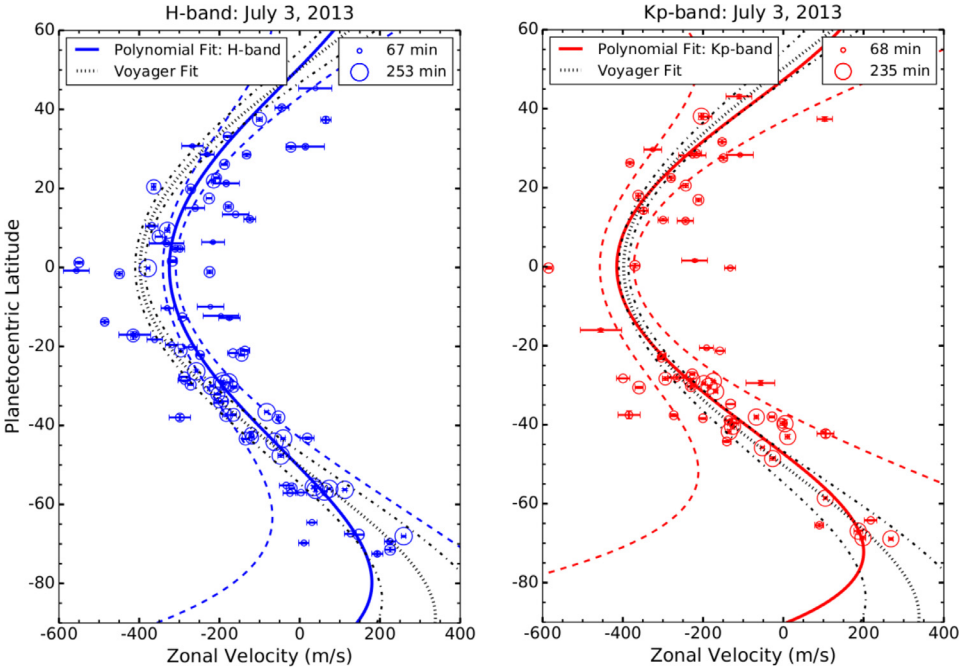

Fig. 9. Eastward zonal wind velocities of tracked features in the H- and K'-band on July 3, 2013. Individual features are plotted as circles with their marker size proportional to the length of time the feature was tracked. The shortest and longest times are given in the top right corner. The Voyager profile is shown in a dotted black line with the width of uncertainty in a dot-dash black line. Our polynomial fit to the H-band is shown with a blue solid line (left image) while the fit to the K'-band is in red (right image). Their widths of uncertainty are in dashed blue and red lines, respectively. There is significant positive deviation in the H-band wind speeds at the equator compared to those derived by the Voyager fit by 73 ± 16 m/s. The K'-band velocities agree well with the Voyager profile. (For interpretation of the references to color in this figure legend, the reader is referred to the web version of this article.)

tions. There is a 93 ± 29 m/s deviation between the H-band and canonical profile and a 141 ± 63 m/s difference between the H- and K'-bands on this night. There is no significant difference between the K'-band and Voyager profile on either night. The difference between the H-band and Voyager profiles qualitatively agree with Fitzpatrick et al. (2014), although their H-band velocities are best described by a profile shifted toward positive velocities by 180 ± 50 m/s. The dispersion of our new results falls within the wide range seen in previous publications. Spreads in feature velocity were first seen in measurements of the motions of small clouds in Voyager 2 data, particularly around the GDS and Dark Spot 2 (Smith et al., 1989; Limaye and Sromovsky, 1991). Martin et al. (2012) found large spreads in zonal velocities at constant latitudes in Keck AO H-band observations. Comparatively, at the southern

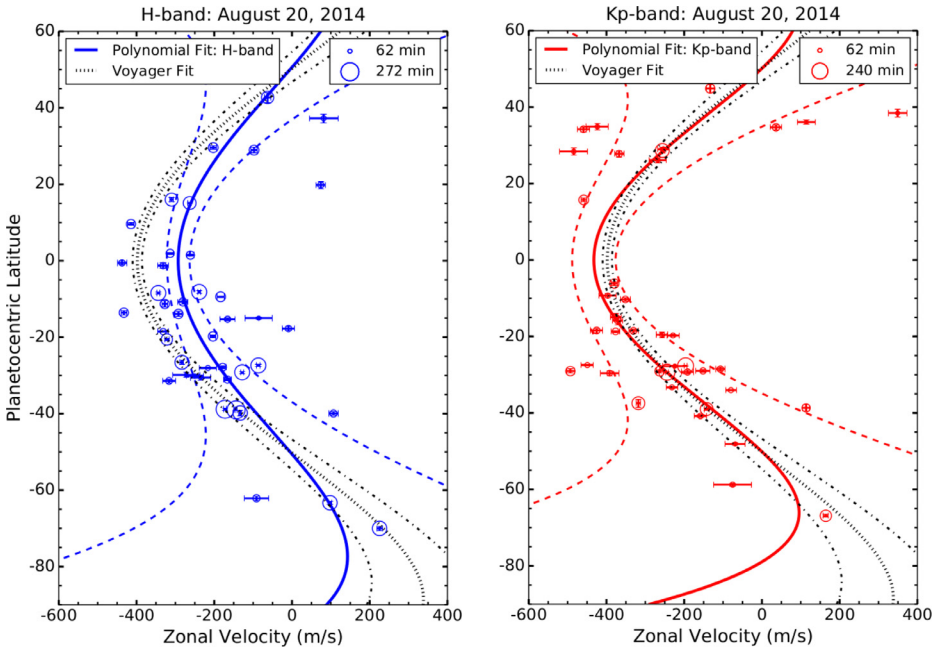

Fig. 10. Same as Fig. 9 except for August 20, 2014. The Voyager profile is shown in a solid black line with the width of uncertainty in a dashed black line. Our polynomial fit to the H-band is shown with a blue solid line while the fit to the K'-band is in red. Again, there is a significant positive shift in the H-band zonal velocities at the equator compared to those derived by Voyager by 93 ± 29 m/s. (For interpretation of the references to color in this figure legend, the reader is referred to the web version of this article.)

Table 1
Parameters in the fits to tracked zonal wind velocities. The fits are 4th-order polynomials given by: $V = a + b\theta^2 + c\theta^4$ (top half). For comparison, profiles generated from 4th-order Legendre polynomial fits given by: $V = a + b(3\mu^2 - 1)/2 + c(35\mu^4 - 30)/8$ where $\mu = \sin\theta$, are also shown (bottom half). The equatorial velocities derived from the Legendre polynomials are all well within the 2-sigma uncertainty given by the generic polynomial fits.

Poly. profile	a (m/s)	b	c
Voyager	−398 ± 12	1.88E−1 ± 1.40E−2	−1.20E−5 ± 3.00E−6
H-band 2013	−325 ± 16	1.58E−1 ± 2.20E−2	−1.21E−5 ± 4.67E−6
K'-band 2013	−415 ± 42	2.35E−1 ± 5.34E−2	−2.23E−5 ± 1.14E−5
H-band 2014	−292 ± 29	1.45E−1 ± 4.91E−2	−1.18E−5 ± 1.11E−5
K'-band 2014	−433 ± 56	2.40E−1 ± 7.88E−2	−2.73E−5 ± 1.90E−5
Leg. profile	a	b	c
H-band 2013	−159	462	37
K'-band 2013	−134	601	−127
H-band 2014	−95	359	76
K'-band 2014	−147	474	13

low- and mid-latitudes, the Voyager data show much less dispersion from the canonical profile than the results of Martin et al. (2012). Fitzpatrick et al. (2014) also observed significant deviation in H-band features at the equator and southern-mid latitudes compared to the Voyager profile, with differences reaching as high as ~500 m/s.

Spurious data affect the fit. Such data could be due to a number of factors including features near the edge of Neptune's circumference becoming smeared from projection, changes in cloud morphology, limb-brightening, navigation errors, and errors in the position extraction procedure. Several features also move in oscillatory patterns (as in Martin et al., 2012) and limited tracking times may not capture a feature's full period of motion. Similar effects were seen on Uranus due to inertial oscillations (Sromovsky and Fry, 2005). Figs. 9 and 10 show the individual feature velocities and their 1σ errors alongside the zonal wind profiles. Each feature's plot symbol is proportional to its tracking time. Features tracked over the entire observing period generally have smaller errors than those tracked in only a few images and tend to lie closer to their band's zonal wind profile. Thus, the spread in feature velocities at a fixed latitude is partially a result of their limited tracking time and measurement errors. Figs. 11 and 12 show features which have velocity errors less than 30 m/s and were tracked in at least 10 images (~2.5 h). These features are usually bright and morphologically stable and are likely to follow the zonal flow. Spreads in feature velocities up to ~200 m/s at constant latitudes are still seen on both nights and both bands, although this is far less than the spread of 500–600 m/s seen with the full set of tracked features. This suggests that large, bright features are less dispersed from the derived zonal profile. It is also true that such features are less susceptible to tracking errors, which might also account for much of their reduced dispersion. This is consistent with Martin et al. (2012), who also found that the brightest features usually agreed with the canonical profile. However, we still find that the H- and K'-bands zonal wind profiles still differ by more than 1σ at the equator. The H-band and canonical profiles also differ by 2σ at the equator.

The meridional wind velocities for each tracked feature are plotted in Figs. 13 and 14. Globally, the latitudinal velocities are consistent with zero. But, a few features have latitudinal velocities as large as 100–200 m/s. The zonal velocity of these features tend to significantly deviate from the canonical profile, suggesting they are driven by mechanisms that produce motion in both directions, such as vortices or wave mechanisms. This behavior was found by Sromovsky et al. (2001a, 2001b, 2001c) in HST observations, where several features near the same longitude as a dark spot, but widely scattered in latitude, were accurately measured (within 10–20 m/s) to have meridional wind speeds around 100 m/s, and zonal winds that deviated from the canonical profile by over 200 m/s, while the vast majority of their tracked clouds had insignificant meridional motions and very small deviations from the canonical profile. However, our features with this behavior also have large errors and are not tracked for very long. As previously mentioned, the centers and velocities of features that are faint, ephemeral, or close to the limb, are difficult to constrain.

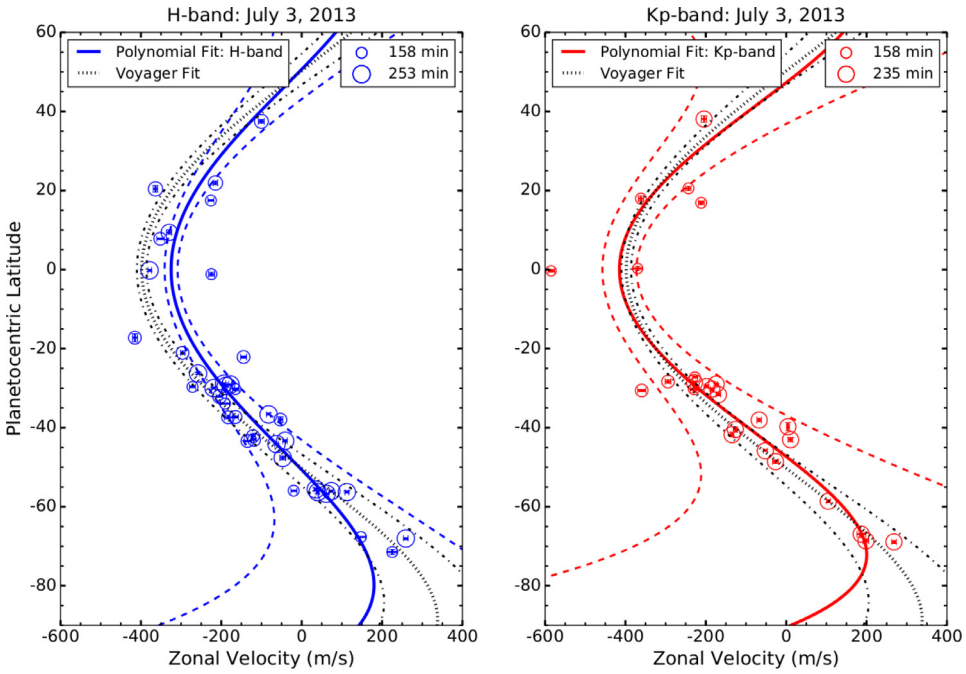

Fig. 11. Same as Fig. 9 but only including features tracked in at least 10 images and with errors <30 m/s.

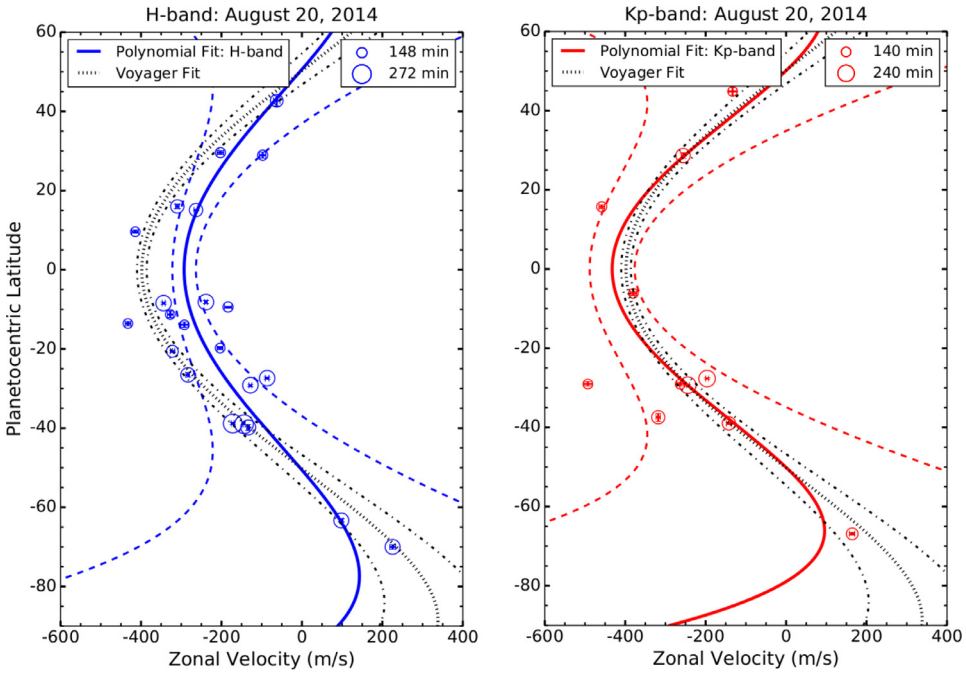

Fig. 12. Same as Fig. 12 but only including features tracked in at least 10 images and with errors <30 m/s.

4.2. Trends in feature depth and velocity

The derived H and K' profiles give a crude 3D look into Neptune's upper atmosphere since these bands probe different altitudes. We hypothesize that the equatorial shift in the H-band profile is due to deep features. Our data are spectrally limited so accurate cloud top pressures cannot be determined. However, the K'-to-H I/F ratio indicates whether features are deeper or shallower relative to one-another: the deeper a cloud is in the atmosphere, the greater the expected H-band intensity relative to the K'-band intensity. We compute the maximum allowed K'-to-H I/F ratio for each 2013 H-band feature and compare this to their latitude and zonal velocity (see Table 5 in Supplementary Materials 1). Uncertainties are estimated as 20% of I/F, from the uncertainty in the photometry. Fig. 15 plots the maximum K'-to-H I/F ratio vs. latitude of each H-band feature. We find equatorial features ($\pm 20°$) have smaller K'/H intensities than those at mid-latitudes, suggesting they are deeper. This is consistent with Fitzpatrick et al. (2014), who found that clouds at equatorial latitudes are uniformly deeper (~0.5 bar) than those at northern mid-latitudes (~0.1 bar). Numerous authors also find northern features at the highest altitudes (Sromovsky et al., 2001b; Gibbard et al., 2003; Luszcz-Cook, 2012; de Pater et al., 2014), generally in the stratosphere at the ~10 mbar level, although exact pressures vary due to spectral limitations,

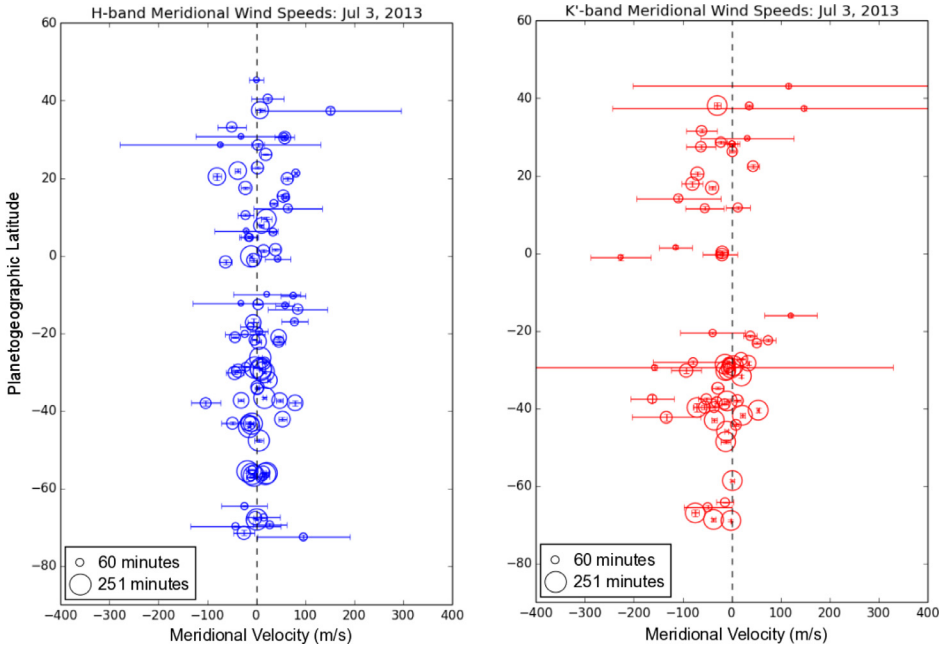

Fig. 13. Meridional velocities of tracked features on July 3, 2013 with the H-band in blue on the left and the K'-band in red on the right. Circle size is proportional to tracked time with the shortest and longest times in the bottom left corners. The black dashed line marks zero and visually shows that the velocities are not too different from zero. (For interpretation of the references to color in this figure legend, the reader is referred to the web version of this article.)

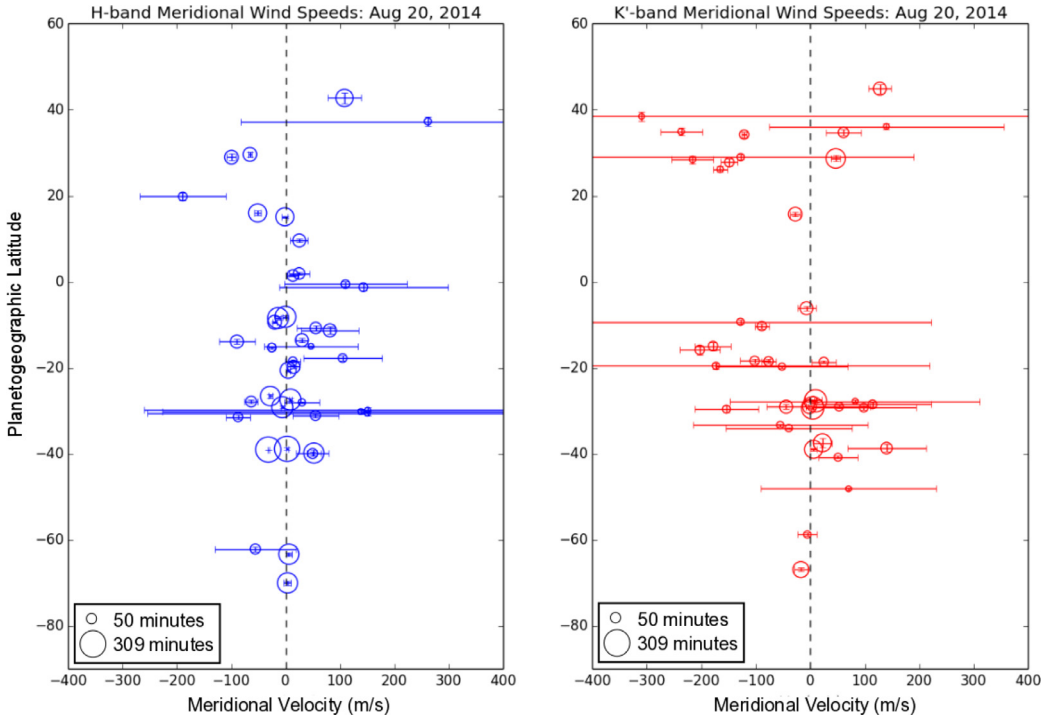

Fig. 14. As Fig. 13 except for August 20, 2014.

instrument sensitivity at different altitudes, and model assumptions. Luszcz-Cook et al. (2010) compared observed and modeled K'/H and K'/J intensities to determine upper altitudes for south polar features and found that a K'/H ratio of 10% gave a minimum cloud top pressure of 0.4 bar. Features seen in H but not K' may also be deep, with pressures greater than 1 bar. A notable example of this is the south polar feature, observed in H-band but not in K', located at 1.6 bar (de Pater et al., 2014). We tracked 29 and 20 H-band features in our 2013 and 2014 observations, respectively, that were equatorward of 20° N/S, but only 10 (in 2013) and 11 (in 2014) K'-band features in this same region. Taken altogether, we argue that the H-band zonal wind profile represents features which are, on average, deeper than those given in the K'-band profile at low latitudes.

Fig. 15 plots the zonal velocity difference from the derived K'-profile vs. latitude for each 2013 H-band features. The difference between the H- and K'-band profiles (from Fig. 9) is overplotted. Positive values indicate velocities eastward (less negative) relative

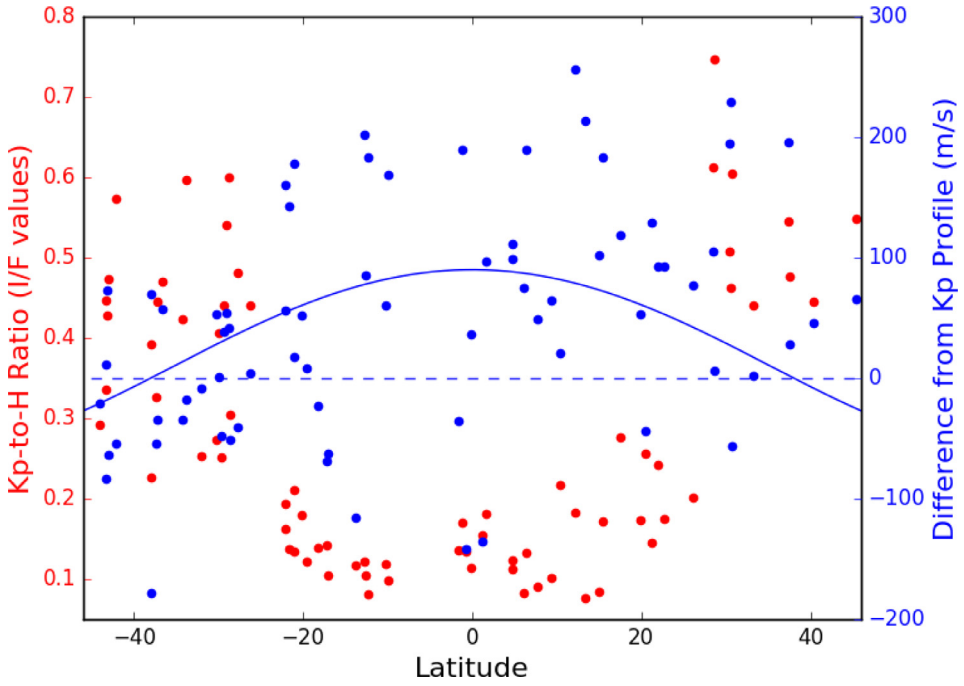

Fig. 15. Derived K'-to-H I/F ratios vs. latitude (red) and zonal velocity deviation from the K' profile vs. latitude (blue) for 2013 H-band features. Shown are features between ±45°. Positive values in velocity variation are eastward (less negative) relative to the K'-profile Overplotted is the difference between the H and K' profiles (solid blue line) and the zero velocity difference (dashed blue line). Features in the equatorial region (±25°) have smaller K'/H intensities and larger velocity variations than those at mid-latitudes. This suggests that the shift in the H profile from the K' and canonical profiles is partly due to deep features. (For interpretation of the references to color in this figure legend, the reader is referred to the web version of this article.)

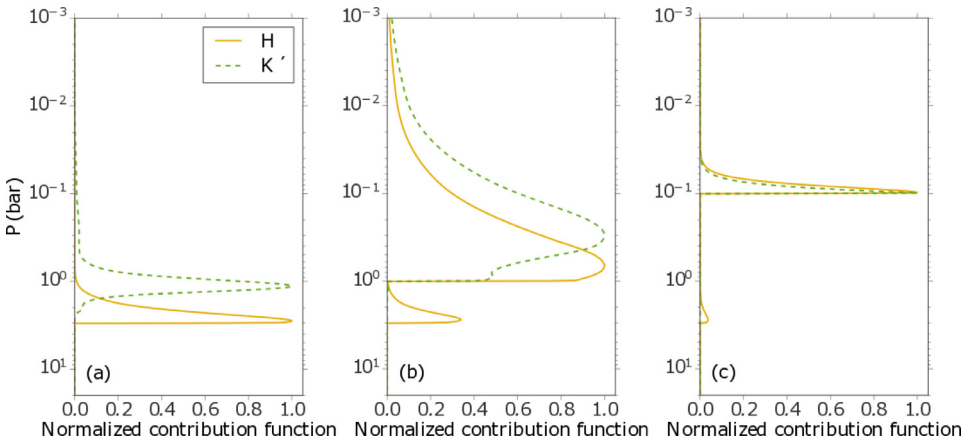

Fig. 16. Normalized H-band (solid orange line) and K-band (green dashed line) contribution functions for three different model atmospheres, illustrating the range of depths from which the H- and K'-reflectivity may arise. In all three cases, gas opacity is contributed by collision-induced absorption of H_2 with H_2, He, and CH_4; and by CH_4 absorption. Details of the atmosphere models may be found in Luszcz-Cook et al. (2016). The three models differ only in the assumed distribution of aerosols: all three models include a vertically thin cloud at 3 bar with a 1.6-micron optical depth of 0.5. In model (a), the atmosphere is clear aside from this 3-bar cloud. In model (b), there is an additional haze (scale height equal to that of the gas) between 1 bar and 1 mbar, with total 1.6-micron optical depth of 0.5. Model (c) includes the 3-bar cloud and an additional vertically thin cloud at 0.1 bar, also with a 1.6 micron optical depth of 0.5. Single scattering albedo and asymmetry factors are 0.75 and 0.7, respectively, for all aerosol particles. (For interpretation of the references to color in this figure legend, the reader is referred to the web version of this article.)

to the K'-profile. The largest deviations from the K' profile are around the equator, where features have low K'/H intensities and are probably deep. The deviations in zonal velocity of features at the southern midlatitudes lie closer to zero and are mostly within the uncertainty of the K' profile fit. This is consistent with our hypothesis: the shift in H-band profile may be driven by a handful of deep features around the equator.

Previous studies have also shown that the brightest H-band features are typically at greater depths (pressures) than the brightest K'-band features (Gibbard et al., 2003; Luszcz-Cook, 2012; de Pater et al., 2014). This is consistent with our expectations from radiative transfer modeling. Fig. 16 shows the contribution functions for each filter in three different atmospheric models, illustrating the range of depths from which the H- and K'- reflectivity may arise. In all three cases, the gas opacity is dominated by H_2 collision-induced absorption and CH_4 absorption. All models include a vertically thin cloud at 3 bar with a 1.6 μm optical depth of 0.5; models (b) and (c) contain additional aerosols in the upper troposphere/stratosphere, as described in the figure caption. For the purposes of our models in the following sections, we assume that the H-band features are located at 1–2 bar, while K'-band features are located between 10–100 mbar.

5. Interpreting differences in the H and K' zonal wind profiles

The major caveat to current and past zonal wind profiles is that they are merely best fits to the data. These fits do not pick up any fine scale structure in the zonal winds. Moreover, the profiles represent features driven by a number of possible mechanisms, including shear, wave phenomena, or other local dynamics. Dispersion is partly due to faint, ephemeral features, whose exact centers and velocities may be difficult to pinpoint. Thus, explaining all variations in zonal velocity from these profiles is difficult, if not impossible, to do.

We also note that our following models assume that the derived zonal flow is set at a constant pressure level. However, tracked features are not necessarily at the same altitude. For instance, northern mid-latitude features appear at the highest altitudes on Neptune (Sromovsky et al., 2001b; Gibbard et al., 2003; Luszcz-Cook, 2012; Fitzpatrick et al., 2014; de Pater et al., 2014). Irwin et al. (2016) analyzed VLT/SINFONI H-band observations made in 2013 and found bright, deep seated clouds ($P > 1$ bar) in the southern mid-latitudes and 'intermediate' clouds ($300 < P < 400$ mbar) in the near-equatorial region. Moreover, features at constant latitudes may have different altitudes. de Pater et al. (2014) saw NIR clouds in the southern midlatitudes at two levels: in the stratosphere from 0.02–0.03 bar and at altitudes below 0.3 bar ($P > 0.3$ bar). Luszcz-Cook (2012) observed similar altitude variations in Keck OSIRIS data.

With these limitations in mind, we only attempt to explain the mean ~100 m/s eastward offset in the equatorial region in the H profile from the canonical and K' profiles. This difference seems real (greater than 2σ) and persistent, seen in 2009 (Fitzpatrick et al., 2014) and now in both our 2013 and 2014 observations. Fry and Sromovsky (2004) also show that H-band wind results from 202 cloud measurements taken in 2003 and 2004 images also fall below the canonical profile at low latitudes. Based on the K'/H intensity trends and previous NIR studies, we interpret the H-band profile in the equatorial region as the "average" zonal velocity of features which are mostly: (1) deep (greater than 1 bar), and (2) have velocities shifted ~+100 m/s from the K'-profile. Likewise, we interpret the K'-band profile in the equatorial region as the "average" zonal velocity of features which are mostly: (1) located in stratosphere (around ~10 mbar), and (2) have velocities shifted ~−100 m/s from the H-profile. Differences in the zonal winds with depth at constant latitude and time is evidence of vertical wind shear in Neptune's troposphere and stratosphere. Our derived profiles suggest a wind shear around −100 m/s over several scale heights at the equator (increasing with height).

The Voyager results of Sromovsky et al. (1993) also provide evidence of vertical wind shear. Fig. 15 shows that three major long-lived cloud features, including the GDS, Scooter, and the Second Dark Spot, all move in the same direction as the canonical profile, but with reduced speed. If these major features are more deeply rooted than the small clouds on which the canonical profile is based, and there is spectral evidence that this is true for Scooter, then it would appear that this is another example of the magnitude of wind speeds increasing (becoming more westward) with altitude. Based on Voyager 2/IRIS temperature retrievals alone, this produces the wrong sign of vertical wind shear in the thermal wind equation, as explained below.

5.1. Modeling vertical wind shear at the equator with the thermal wind equation

In this section, we will examine the plausibility of vertical wind shear modeled with the thermal wind equation as an explanation for the observations. The largest and most meaningful differences (i.e. smallest uncertainty) between the H- and K'-band zonal wind profiles occur at the equator. In the following text, we discuss the applicability of the thermal wind equation to Neptune and how it may be extended to the equator under certain conditions, despite the Coriolis force vanishing there. Using plausible depths for the H- and K'-band profiles, discussed in the previous section, we then show that integrating the thermal wind equation does not reproduce the predicted vertical wind shear at the equator. Finally, we discuss the importance of methane variability in modeling the vertical wind shear and how it can reconcile the inconsistency between the observed wind shear and the thermal wind equation. We stress that these results are speculative since they rely on assumptions about the symmetric structure of the zonal wind and temperature fields as well as the exact pressures of H- and K'-band features.

Table 2
List of variables and their values (if constant) used in the thermal wind equation.

Variable	Description	Value
Ω	Rotation rate of Neptune (rad/s)	1.09E−4
g	Gravitational acceleration (m/s^2)	11.15
r_0	Neptune's equatorial radius (m)	2.4766E7
H	Scale height (km)	19.1 below 500 mbar 51.8 above 500 mbar
T	Temperature (K)	
u	Zonal velocity (m/s)	
θ	Latitude (rad)	
z	Radial distance into atmosphere (m)	

The standard thermal wind equation is:

$$f_0 \sin\theta \frac{\partial u}{\partial r} = -\frac{g}{r_0 T}\frac{\partial T}{\partial \theta}, \tag{4}$$

where $f_0 \equiv 2\Omega_0$ is the Coriolis parameter at the North Pole, rather than the local Coriolis parameter. We define: r_0 as the radius of the planet, T as the temperature, $\partial T/\partial\theta$ as the latitudinal-temperature gradient as constant pressure P, g as the gravity in the $\hat{\mathbf{r}}$ direction, and u is the zonal (longitudinal) velocity (see Table 2 for values for Neptune).

Although the standard thermal wind equation is used in many planetary atmospheric applications and is derived in many texts, c.f., (Pedlosky, 1987), it is limited in its use due to the divergence of the Coriolis force near the equator. Marcus et al. (2018) derive an equatorial thermal wind equation (EQTWE) which provides a relationship between the vertical wind shear and the horizontal temperature gradients that is valid at and near the equator:

$$f_0 \frac{\partial u}{\partial r} = -\frac{g}{r_0 T}\frac{\partial^2 T}{\partial \theta^2} \tag{5}$$

A similar result was noted as Eq. (8.2.2) in Andrews et al. (1987). This equation is derived by assuming $\partial T/\partial\theta \equiv 0$ and taking L'Hôspital's rule of the standard thermal wind equation in the limit as $\theta \to 0$. One problem with using L'Hôspital's rule in this fashion is that it creates a singularity at the equator if $\partial T/\partial\theta \neq 0$ there. The EQTWE derived by Marcus et al. (2018) does not require mirror-symmetric flow and does not produce this singularity.

It is seen by inspection that integrating both (4) and (5) upward will not reproduce the observed H and K'-band equatorial differences. As the zonal winds become more negative (westward) with altitude (H-band to K'-band), $du/dr < 0$. This implies that the meridional temperature gradient and its second derivative at the equator to mid latitudes must be positive. However, this is inconsistent with derived temperature profiles of Neptune's troposphere from Voyager/IRIS spectra in Fig. 17, which show that the equator and poles are warm and the mid-latitude are cool and $\partial^2 T/\partial\theta^2 < 0$ at the equator. (Fletcher et al., 2014).

In the next two sections, we discuss two reasons that could reconcile the inconsistency between the derived zonal wind pro-

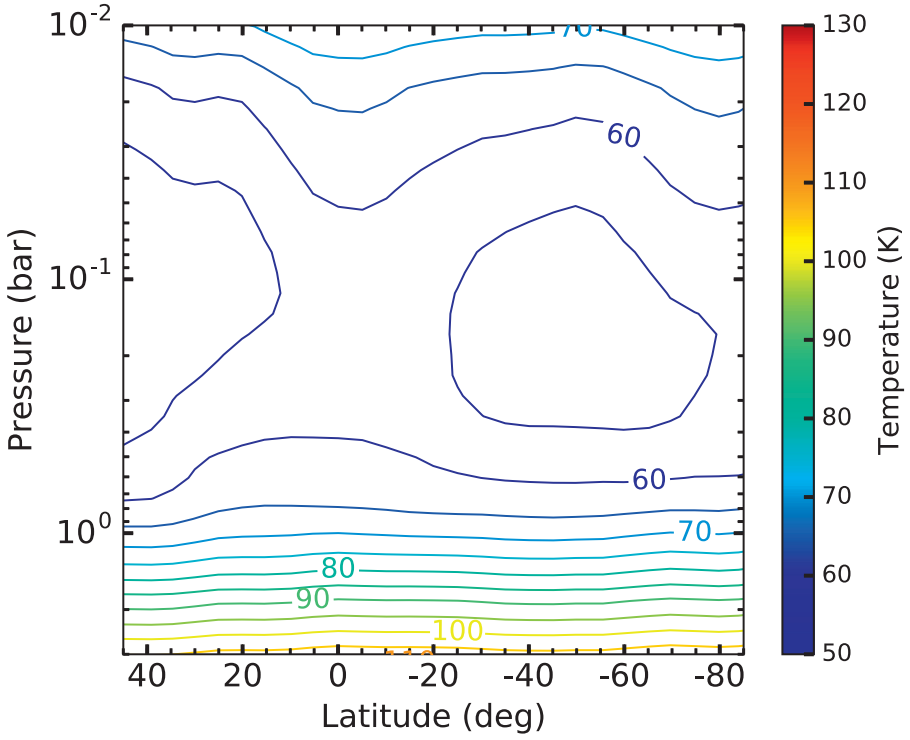

Fig. 17. Temperature contours from inbound Voyager/IRIS spectra (Conrath et al., 1991; Fletcher et al., 2014). This profile was used to determine the meridional temperature gradient.

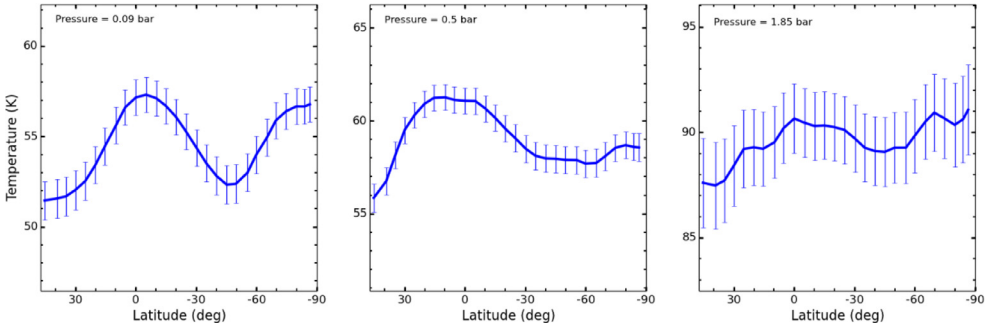

Fig. 18. Meridional temperatures and errors at constant pressure from Fletcher et al. (2014). The first two images show Voyager/IRIS temperature retrievals that are within its sensitivity range (70–800 mbar). The latter figure is a temperature profile extrapolated from Voyager/IRIS results by the application of the smooth relaxation to an *a priori* profile. In this case, the uncertainty is substantial.

files and temperature profile. First, we discuss whether the assumed temperature profile is correct. Second, we examine the impact non-ideal gas behavior has on the thermal wind equation. In particular, we focus on the latter (our preferred) explanation in the subsequent discussion.

5.1.1. Temperature profile incorrect?

Our temperature data come from inbound Voyager/IRIS maps, which are only sensitive to the 70–800 mbar range (Conrath et al., 1991; Fletcher et al., 2014). Temperatures above and below these pressures are smooth relaxations to an *a priori* profile based on the mean stratospheric temperature and the profile from Moses et al. (2005). So, while average global temperatures are known throughout the upper atmosphere, the meridional trends are more uncertain outside 70–800 mbar. This can be seen in the data itself. In Fig. 18, we plot sample inbound temperature data with error bars inside and outside the 70–800 mbar range. At pressures outside this range, the uncertainties become larger, approaching the temperature difference between the equator and mid-latitudes. We cannot confidently infer whether the equator is warmer or colder than the mid-latitudes outside 70–800 mbar from the current data alone.

We now explore whether meridional variations in temperature outside the well-constrained 70–800 mbar pressure range could cause wind shear consistent with the difference between our H and K' observations. We break this calculation into two steps.

First, we calculate the wind shear du/dr between the depth of the K'-band profile down to 1 bar. We do this by using the temperature profile given by the Voyager/IRIS spectra (Fig. 17) to determine the expected zonal wind profile at 1 bar assuming the K'-profile is at a set pressure level. Since the depth of the K' features are not precisely constrained, we test a range of pressures from 10 to 100 mbar. The value du/dr is the difference in the zonal winds between the extrapolated profile at 1 bar and the H-band, which we also set to a variety of pressures between 1.0–2.4 bar, 2.4 bar being the location of a commonly assumed optically thick bottom cloud (Irwin et al., 2011). Altitude changes are calculated assuming hydrostatic equilibrium with a scale height of 19.1 km in the troposphere and lower stratosphere, a value obtained from de Pater et al. (2014). Voyager/IRIS derived meridional temperatures are

Table 3
Examples of the errors in the temperature fit to that derived from Voyager/IRIS spectra as a function of pressure and fit degree N. The l^1-norm is the sum of the absolute difference between the observed and modeled data and the l^2-norm is the sum of the squares of these differences.

Pressure (bar)	N	l^1-norm	l^2-norm
0.1	2	16.6724	14.4143
0.1	4	11.3805	8.1870
0.1	6	10.8843	7.0204
0.1	8	14.1867	10.2813
0.01	2	41.0348	81.8547
0.01	4	26.0158	39.5551
0.01	6	25.6478	37.7382
0.01	8	28.2277	39.3755

sampled every 5° latitude, which is too sparse to reliably numerically differentiate. To circumvent this issue, we fit a symmetric profile to the temperature data:

$$T(\theta) = \sum_{n=0}^{N} a_n \cos(n\theta) \tag{6}$$

One problem with this assumption is evidence of seasonal variations in Neptune's atmospheric brightness that could cause differences in hemispheric temperatures (Sromovsky et al., 2003; Hammel and Lockwood, 2007). Fletcher et al. (2014) and de Pater et al. (2014) estimate random uncertainty in the Voyager/IRIS temperatures to be 1–2 K in the troposphere, increasing to 2–4 K in the mid-stratosphere. The temperature difference predicted from Voyager/IRIS between hemispheres at constant latitude is close to or within this error, so our chosen temperature profile is consistent with meridional symmetry. We now evaluate the derivative of (6) divided by $\sin\theta$:

$$\frac{1}{\sin\theta}\frac{\partial T}{\partial \theta} = -\frac{1}{\sin\theta}\sum_{n=1}^{N} n a_n \sin(n\theta) \tag{7}$$

$$= -\sum_{n=1}^{N} n a_n [\sin(n\theta)/\sin\theta] \tag{8}$$

It can be shown that the ratio of sines in the summation is:

$$\sin(n\theta)/\sin\theta = \begin{cases} 2[\cos((n-1)\theta) + \cos((n-3)\theta) + \cdots \\ \quad + \cos(3\theta) + \cos(\theta)] : n \text{ even} \\ 2[\cos((n-1)\theta) + \cos((n-3)\theta) + \cdots \\ \quad + \cos(4\theta) + \cos(2\theta) + 1/2] : n \text{ odd} \end{cases}$$

We substitute the above expression and Eqs. (6) and (7) into Eq. (4) to obtain a numeric thermal wind equation.

One problem with this formulation is that the coefficient a_N with the highest order will contribute the most to the derivative at lower latitudes. To mitigate this effect, we must fit the temperature to as low an order as possible while maintaining a reasonable fit. Table 3 compares various errors of the fit to the observed temperature data as a function of pressure and fitting degree. We choose to use $N = 4$ which is the lowest order that provides a reasonable fit to the temperature data.

Second, we solve for the meridional temperature structure needed to reproduce the vertical wind shear between the 1 bar zonal wind profile (calculated in the first step) and that at the pressure of the H-band profile. This is done by integrating (4) and (5) and solving for $T(\theta, P)$. We choose 1 bar as the upper limit to the constructed temperature profiles for two reasons: (1) from de Pater et al. (2014), the equatorial H-band features not seen in K' must be below 1 bar; (2) if we placed our limit at the edge of the Voyager/IRIS range, unphysical discontinuities in the temperature structure would arise. Placing the limit at 1 bar allows reasonable 'smoothing' in the temperature structure between 800 mbar and 1 bar.

Away from the equator, we solve for the meridional temperature structure with the standard thermal wind equation where we integrate this equation with respect to a reference latitude θ_0 at a particular pressure P:

$$2\Omega \int_{\theta_0}^{\theta} \sin\theta' \frac{du(\theta', P)}{dr} d\theta' = -\frac{g}{r_0}\int \frac{1}{T(\theta, P)} dT, \tag{9}$$

and then solve for $T(\theta, P)$:

$$\log\left(\frac{T(\theta, P)}{T_0(P)}\right) = -\frac{2\Omega r_0}{g}\int_{\theta_0}^{\theta} \sin\theta' \frac{du(\theta', P)}{dr} d\theta'. \tag{10}$$

Here, $T_0(P)$ is the temperature at θ_0. The extrapolated zonal wind profile at 1 bar from the K'-band profile can be fit to a fourth-order polynomial in degrees latitude, as was done with the H- and K'-band profiles. So, the total vertical wind shear can be written as:[2]

$$\frac{\partial u}{\partial r} = p_0 + p_1 \cdot \theta^2 + p_2 \cdot \theta^4 \tag{11}$$

Note that θ is converted from degrees to radians for the purposes of integration. Furthermore, this procedure assumes du/dr is constant with pressure (although still a function of latitude) so the resultant temperature structure will represent an 'average' profile. p_0, p_1, and p_2 do not depend on latitude (though they depend on the pressure the K'-band is placed). Eq. (9) becomes:

$$\log\left(\frac{T(\theta, P)}{T_0(P)}\right) = -\frac{2\Omega r_0}{g}\int_{\theta_0}^{\theta} \sin\theta' \frac{du(\theta', P)}{dr} d\theta' \tag{12}$$

$$= -\frac{2\Omega r_0}{g}\int_{\theta_0}^{\theta} \sin\theta' \left(p_0 + p_1\theta'^2 + p_2\theta'^4\right) d\theta' \tag{13}$$

The integral on the right-hand side of can be solved analytically via repeated integration-by-parts. The final solution, written for brevity, is:

$$\log\left(\frac{T(\theta, P)}{T_0(P)}\right) = -\frac{2\Omega r_0}{g}(p_0 \cdot t_0 + p_1 \cdot t_1 + p_2 \cdot t_2) \tag{14}$$

$$T(\theta, P) = T_0(P) \cdot \exp\left[-\frac{2\Omega r_0}{g}(p_0 \cdot t_0 + p_1 \cdot t_1 + p_2 \cdot t_2)\right] \tag{15}$$

where:

$$t_0 = -\cos\theta$$
$$t_1 = 2\theta\sin\theta - (\theta^2 - 2)\cos\theta$$
$$t_2 = 4\theta(\theta^2 - 6)\sin\theta - (\theta^4 - 12\theta^2 + 24)\cos\theta$$

At and near the equator, we use the EQTWE to solve for the thermal profile. Assuming the same model for the vertical wind shear (35), the EQTWE becomes a second-order differential equation in θ:

$$T'' = c \cdot p(\theta) T, \tag{16}$$

[2] We use fourth-order polynomial fits in latitude to the vertical wind shear, instead of Legendre polynomials in $\sin\theta$ for two reasons. First, while the solution to Laplace's equation on a sphere are expressed in terms of Legendre polynomials in $\sin\theta$ (and are used to fit the zonal wind profile for Uranus in Sromovsky et al., 2009), this is only especially necessary close to the poles, whereas we are doing a local expansion near the equator. Second, we feel it best to use fourth-order fits in latitude since this is the most common fit in the literature to the zonal wind profiles for Neptune. In the Appendix, we show an example demonstrating that using a Legendre expansion does not change the qualitative interpretation of the temperature profile from the equator to mid-latitudes.

where $p(\theta) = p_0 + p_1\theta^2 + p_2\theta^4$ and $c = -f_0 r_0/g$. Letting T to be symmetric about the equator:

$$T = \sum_{n=0}^{\infty} a_{2n}\theta^{2n}. \tag{17}$$

Then:

$$T'' = \sum_{n=1}^{\infty} a_{2n}(2n)(2n-1)\theta^{2n-2} \tag{18}$$

Change the limits on (18):

$$T'' = \sum_{n=0}^{\infty} a_{2n+2}(2n+2)(2n+1)\theta^{2n}. \tag{19}$$

Plug these expansions into (16):

$$\sum_{n=0}^{\infty} a_{2n+2}(2n+2)(2n+1)\theta^{2n} = c \cdot p(\theta) \sum_{n=0}^{\infty} a_{2n}\theta^{2n} \tag{20}$$

$$\sum_{n=0}^{\infty} (a_{2n+2}(2n+2)(2n+1) - a_{2n}c \cdot p(\theta))\theta^{2n} = 0 \tag{21}$$

The above implies that the relation within the parentheses equals zero for all powers of θ. The only complication is that $p(\theta)$ also include powers of θ. The recurrence relation for the constants are below:

$$a_2 = a_0 \frac{c \cdot p_0}{2} \tag{22}$$

$$a_4 = a_2 \frac{c \cdot p_1}{12} \tag{23}$$

$$a_6 = a_4 \frac{c \cdot p_2}{30} \tag{24}$$

$$a_{2n+2} = a_{2n} \frac{c}{(2n+2)(2n+1)} \tag{25}$$

a_0 is the equatorial temperature. As an example, set $a_0 = 80$ K and plug in relevant values of the constants for Neptune. Then (4) becomes:

$$T = 80 + 28.7\theta^2 - 13.4\theta^4 - 0.1\theta^6 + \cdots \tag{26}$$

To summarize, we have calculated the thermal structure below 1 bar by solving both the standard and equatorial thermal wind equations. The latter is valid at and near the equator while the former is valid away from it. Assuming an equatorial temperature of 80 K, we find that the difference between the modeled temperatures resulting from these two models is 0.5 K at ±20° and 0.2 K at ±15°. The reason the temperature solution given in (15) is almost equal to the solution given by (26) near the equator is that (15) is symmetric about the equator (t_0, t_1, and t_2 are all even functions). Thus, in the limit as θ goes to 0, the solutions appear similar near the equator due to L'Hôspital's rule.

Fig. 19 shows a contour plot of a temperature profile in Neptune's troposphere that matches the observed H- and K'-band wind profiles through the thermal wind equation. The Voyager/IRIS temperature retrievals are plotted for pressures less than 800 mbar. The temperature solution required to match the observed equatorial vertical wind shear is shown for pressures greater than 1 bar. We choose the reference latitude θ_0 to be the equator and $T_0(P)$ to be the mean global temperature (given by the smooth relaxation to the *a priori*) at P. In this example, we assumed the K'-band profile corresponds to 10 mbar and the H-band profile represents the 1.3 bar layer. This solution predicts 10–15 K temperature differences between the equator and mid-latitudes below 1 bar. In cases where the H- and K'-band features are further apart in altitude, we predict amplitudes of around 5–10 K at $P > 1$ bar. Requiring these large temperature contrasts has an effect on the IRIS flux and will worsen the quality of the spectral fits. This can be avoided if the H-band profile is moved further outside the IRIS sensitivity window, say $P > 2$ bar. In this case, the quality of the spectral fit is unaffected, but this may result in unrealistic depths for H-band features.

The predicted temperature profile is largely a function of the expected wind shear. Fig. 19 represents an altitude change over 4 scale heights. In cases where the H- and K'-band features are further apart, the temperature contrasts are decreased. If the zonal winds change more rapidly with increasing altitude, larger meridional temperature gradients are needed to match the predicted vertical wind shear. If vertical wind shear is not uniform throughout the atmosphere, then the amplitude of temperature variability will change. For instance, if du/dr changes more rapidly below 1 bar than above it, then there is a larger total integral of $dT/d\theta$ between the H-band and 1 bar. This would decrease the latitudinal gradient needed to produce the expected vertical wind shear and could result in temperature contrasts more compatible with expected IRIS spectral fits.

5.1.2. Revisiting the thermal wind equation

The standard thermal wind equation is derived from the vorticity equation in part by assuming the ideal gas law for a single-component gas: $P = \rho RT$. This involves replacing the horizontal gradient of the density with the horizontal temperature gradient. Therefore in a multi-component atmosphere, the thermal wind equation is not correct because the atmosphere's density gradient is due to spatial variations in temperature and in the composition. The later no longer makes the gas constant 'constant' spatially, but turns it into a function of the densities of the components. Generally, in the Earth's atmosphere, the correction to the thermal wind equation is not large because the molar mass of water (the most significant contributor to density variations in the atmosphere) is small compared to the atmosphere's mean molar mass. However the mean molar mass of the atmosphere of Neptune (and the other giant gas planets) is small compared to the molar mass of gases such as methane that cause spatial density variations. If this effect is large enough to produce significant variations in the meridional density, the thermal wind Eq. (4) will be altered. We define the *virtual temperature* T_v as the temperature at which a dry atmosphere has the same density and total pressure as an atmosphere with an additional component (Sun et al., 1991):

$$T_v = \left(1 + \frac{1-\epsilon}{\epsilon}\frac{q}{1+q}\right)T \approx \left(1 + \frac{1-\epsilon}{\epsilon}q\right)T \tag{27}$$

Here, $q = \rho_c/\rho_d$ is the mass mixing ratio between the extra constituent and dry air and $\epsilon = m_c/m_d$ is the ratio of the molar mass of methane to the molar mass of dry air. For Neptune with methane as the main trace gas, $m_c/m_d \approx 6.96$ and the virtual temperature is:

$$T_v = (1 - 0.856q)T \tag{28}$$

Contrast this with Earth, where water vapor is the main condensible; $m_c/m_d \approx 0.622$ and the virtual temperature is:

$$T_v = (1 + 0.608q)T \tag{29}$$

The atomic mass of methane is larger than that of dry air on Neptune, while the atomic mass of water vapor is smaller than dry air on Earth. Thus, the virtual temperature will be smaller than the actual temperature on Neptune, while the virtual temperature is larger on Earth. An equator enhanced in methane (and with larger q) compared to mid-latitudes will, therefore, have a cold virtual temperature relative to the mid-latitudes. If the density gradient

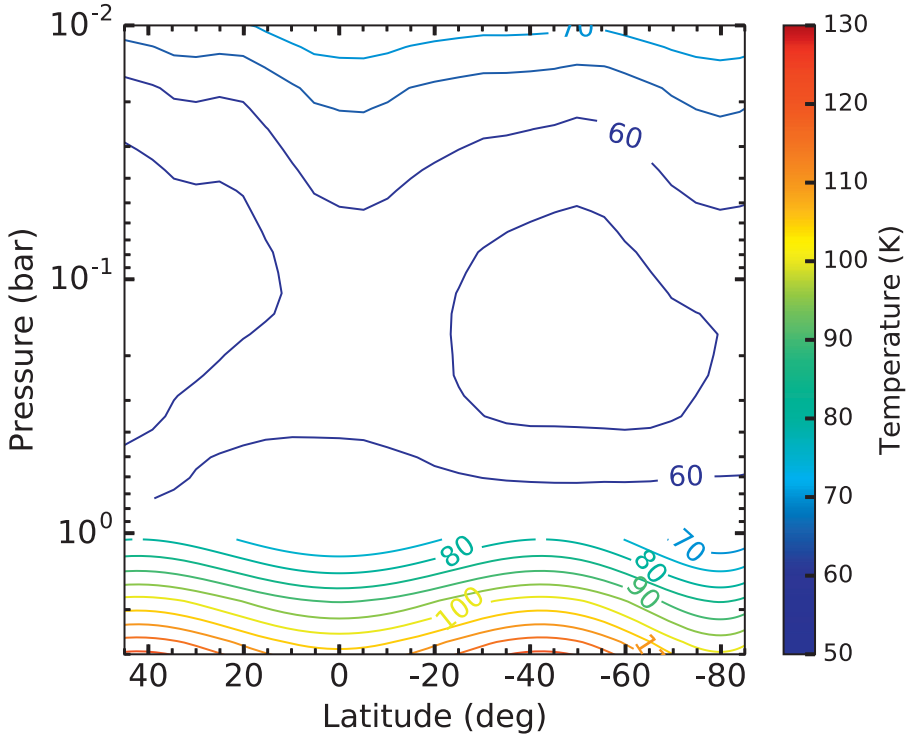

Fig. 19. An example of the derived temperature profiles below 1 bar needed to produce the expected zonal wind differences between the H-and K'-bands. At a given pressure, the temperature at the equator was set to the mean global temperature. This is superimposed with the Voyager/IRIS temperature retrievals above 800 mbar. The region between 800 mbar to 1 bar region is left blank (without a temperature solution) to emphasize that a smooth transition between the solution profile and the Voyager/IRIS profile is needed to avoid unphysical boundaries. For this example, the H-band profile was set at 1.3 bar and the K'-band profile at 10 mbar. In all tested solutions, the required difference between the equatorial and mid-latitude temperatures falls between 5–15 K.

induced by methane abundance variations is large enough, it may explain the sign of Neptune's apparent vertical wind shear.

Sun et al. (1991) use the concept of virtual temperature to derive a more general thermal wind equation. We similarly generalize Eq. (4) by using virtual temperature:

$$f\frac{\partial u}{\partial r} = -\frac{g}{r_0 T_v}\frac{\partial T_v}{\partial \theta}\bigg|_{P,\phi} \tag{30}$$

Defining $C = (1-\epsilon)/\epsilon$, Sun et al. (1991) show that:

$$f\frac{\partial u}{\partial z} = -\frac{g}{r_0 T}\frac{\partial T}{\partial \theta} - \frac{g}{r_0}\frac{C}{1+Cq}\frac{\partial q}{\partial \theta} \tag{31}$$

Eq. (31) is identical to Eq. (7) of Sun et al. (1991), which we refer to as the thermal and compositional wind equation. Their study investigated the effect of horizontal variations in molar mass on vertical wind shear in Neptune and Uranus. They found that methane depletion at high latitudes compared to low latitudes produced vertical wind shear with opposite sign to vertical wind shear produced by thermal gradients. If the gradient in molar mass is large enough to overcome the thermal term, the zonal wind speed will become more negative with increasing altitude, consistent with our observations.

Similar to the previous section, we ask what temperature gradient is needed below 1 bar if molar mass gradients also contribute to the vertical wind shear. Karkoschka and Tomasko (2011) found evidence of methane depletion between 1.2 and 3.3 bar at the mid-latitudes in data acquired by the Hubble STIS spectrograph. They derived a methane molar mixing ratio of 0.04 (0.28 mass mixing ratio) at the equator and a ~3 × depletion at mid-latitudes. Luszcz-Cook et al. (2013) found brightness variations in spatially resolved millimeter maps of Neptune, suggestive of meridional opacity variations. Their models were consistent with methane from 1–4 bar depleted by 2 × at mid-latitudes and by 8 × at the poles compared to nominal values at the equator (0.044 molar mixing ratio). Luszcz-Cook et al. (2016) also find methane variations consistent with Karkoschka and Tomasko (2011). We assume methane is the major source of molar mass variations and that these variations are confined to altitudes below 1 bar but do not otherwise depend on the pressure. We also assume the variation is hemispherically symmetric in order to extend the general thermal wind equation to the equator. Our model reflects the findings of Karkoschka and Tomasko (2011) and is similar to their Fig. 8: methane is enriched at the equator, smoothly decreasing to 45°S and remaining constant out to the poles. The model for the methane mass mixing ratio is expressed below:[3]

$$q(\theta) = \begin{cases} q_0\cos(4\theta) + q_1: & |\theta| \le 45 \\ q_1 - q_0: & |\theta| > 45 \end{cases}$$

Fig. 20 plots our methane model assuming × 2 and × 4 depletion at the mid-latitudes to poles assuming an equator with a molar mixing ratio of 0.04. Fig. 21 plots the virtual temperature assuming this model for the methane mixing ratio. The molecular mass variation due to methane will change the thermal contribution to the observed vertical wind shear. The new equation to solve is:

$$2\Omega\sin\theta\frac{\partial u}{\partial r} = -\frac{g}{r_0 T}\frac{\partial T}{\partial \theta}\bigg|_P - \frac{g}{r_0}\frac{C}{1+Cq}\frac{\partial q}{\partial \theta}\bigg|_P, \tag{32}$$

where we integrate this equation to solve for $T(\theta, P)$:

$$-\frac{g}{r_0}\int\frac{1}{T(\theta,P)}dT = 2\Omega\int_{\theta_0}^{\theta}\sin\theta'\left[\frac{du(\theta',P)}{dr} + \frac{g}{r_0}\frac{C}{1+Cq}\frac{\partial q}{\partial \theta'}\right]d\theta', \tag{33}$$

[3] Among many functions we could choose to represent the methane gradient, we picked $\cos(4\theta)$ since its derivative is zero at 45°. This produces a smooth transition in the methane abundance from low-latitudes and high-latitudes, where methane abundance is constant as in Karkoschka and Tomasko (2011).

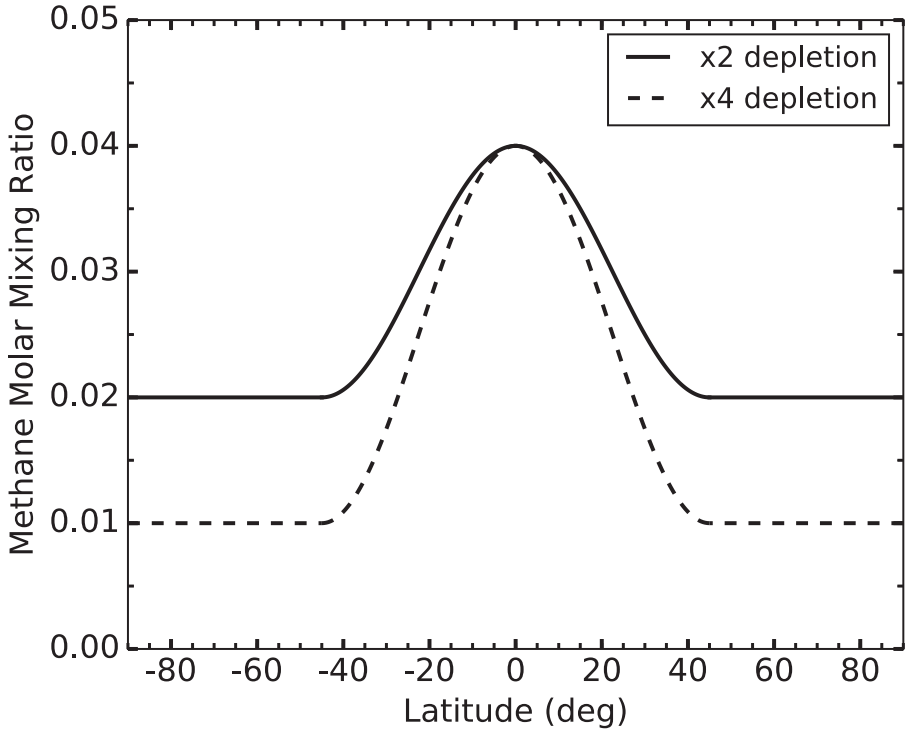

Fig. 20. Plot of our methane model, given by Eqs. (22) and (23).

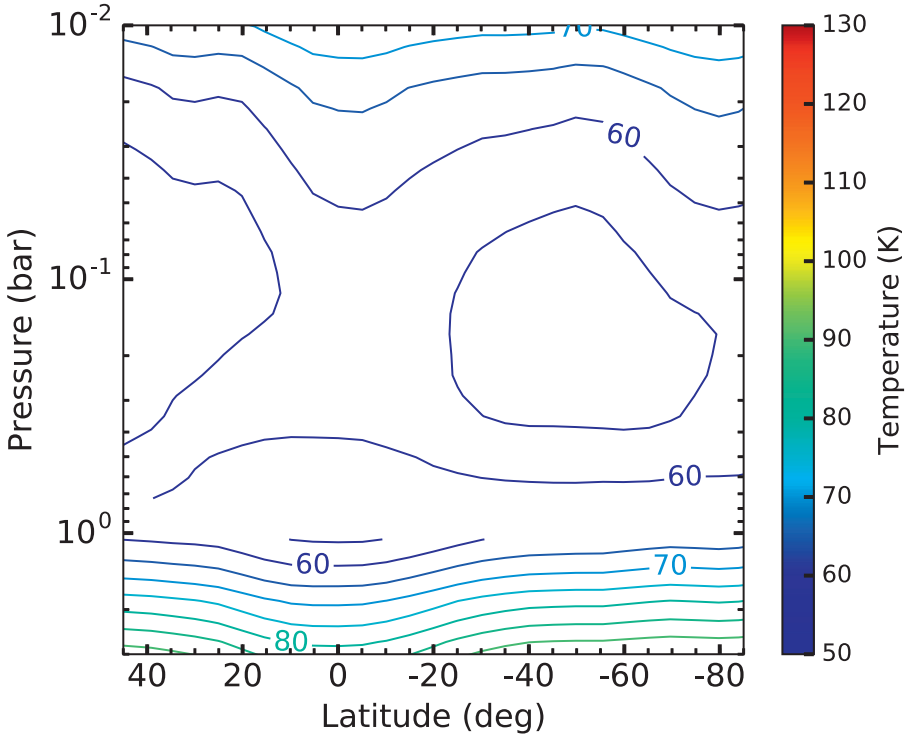

Fig. 21. As Fig. 17, except plotting the virtual temperature below 1 bar, assuming ×2 depletion in methane at mid-latitudes and the poles. The virtual temperature is given by Eq. (28) and demonstrates the impact of methane gradients. A cold virtual temperature at the equator is produced, which is consistent with the expected sign of vertical wind shear.

$$\log\left(\frac{T(\theta,P)}{T_0(P)}\right) = -\frac{2\Omega r_0}{g}\int_{\theta_0}^{\theta}\sin\theta'\left[\frac{du(\theta',P)}{dr} + \frac{g}{r_0}\frac{C}{1+Cq}\frac{\partial q}{\partial\theta'}\right]d\theta' \tag{34}$$

Like before, we assume the vertical wind shear and molar mass term can be fit to fourth-degree polynomials:

$$\frac{\partial u}{\partial r} + \frac{g}{r_0}\frac{C}{1+Cq}\frac{\partial q}{\partial\theta} = p_0 + p_1\cdot\theta^2 + p_2\cdot\theta^4 \tag{35}$$

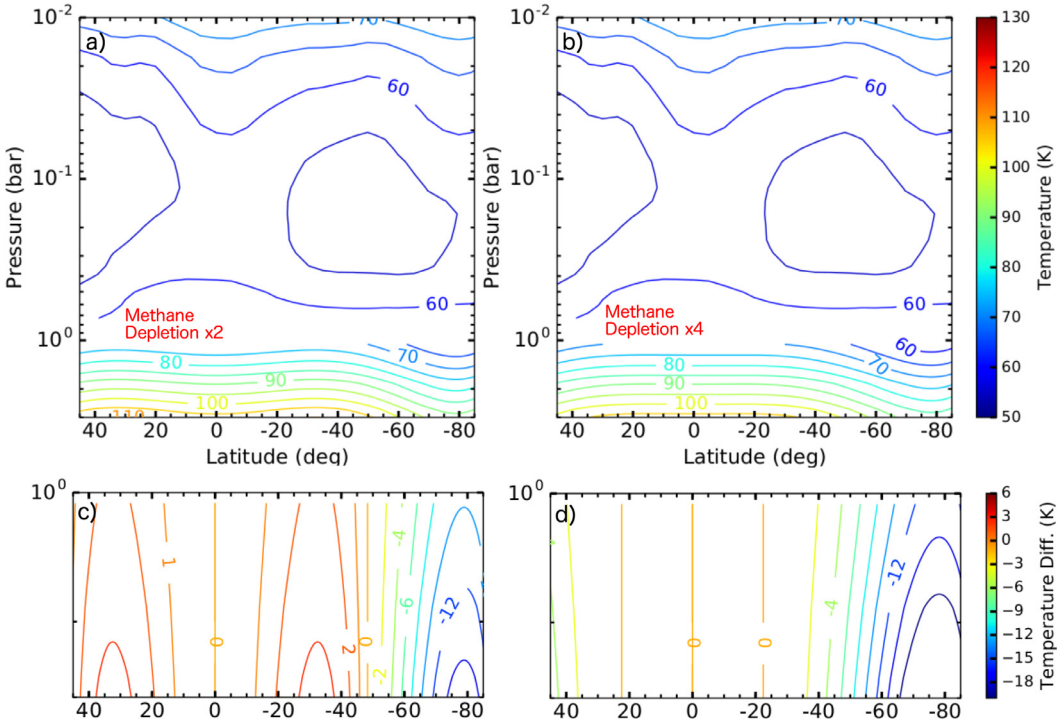

Fig. 22. As Fig. 19, but considering meridional methane variations in the thermal wind equation. (a) Methane abundance depleted by 2 × at mid-latitudes and poles (molar mixing ratio 0.02) compared to the equator (molar mixing ratio 0.04). (b) Methane abundance depleted by 4 × at mid-latitudes and poles (molar mixing ratio 0.01) compared to the equator and (molar mixing ratio 0.04). (c) and (d) show how the derived meridional temperatures deviate from the equatorial temperature along isobars, between 1–3 bar. (c) corresponds to (a) and (d) to (b). The low methane depletion (2 ×) case predicts an equator 2–3 K cooler than the mid-latitudes. Higher depletion (4 ×) yields an equator 2–3 K warmer than the mid-latitudes. These examples highlight how the meridional methane distribution affects the temperature gradient. In both cases, the H-band profile was set at 1.3 bar and the K'-band profile at 10 mbar.

Integrate as before to solve for the temperature profile below 1 bar. The derived temperature profile taking methane variations into account is shown in Fig. 22. Our examples illustrate how important the meridional methane distribution is on the derived temperature solutions. In the first case, where methane is depleted by 2 × at mid-latitudes and poles compared to the equator, we obtain an equator 2–3 K colder than the mid-latitudes. In the second case, where methane is depleted by 4 × at the mid-latitudes compared to the equator and poles, we obtain an equator 2–3 K warmer than the mid-latitudes. This is qualitatively consistent with the warmer equatorial temperatures observed at $P < 1$ bar by Voyager/IRIS (e.g. Conrath et al., 1998) and ground-based observations (Fletcher et al., 2014).

An important caveat to this analysis is that it assumes methane does not condense. Ices are 1000-fold denser than gases and the ideal gas law is no longer applicable. Our model occurs in the heart of methane's condensation region so these results should be viewed with caution. Nonetheless, the above work demonstrates the necessity of including compositional gradients in models of Neptune's winds. Future models will need to consider all phases of methane and other heavy species deeper down to accurately calculate Neptune's density profile.

In summary, the meridional temperature structure needed to replicate Neptune's equatorial zonal wind shear depends heavily on the gaseous methane distribution below 1 bar. If methane abundance is globally uniform or weakly varying, then a cold equator relative to the mid-latitudes is needed to explain the vertical wind shear. If methane abundance changes greatly, then a warm equator is permitted.

Thermal infrared spectra from Cassini/CIRS observations have been used to derive temperature fields for the stratosphere and troposphere of Jupiter and Saturn and allow us to compare our derived temperatures for Neptune's troposphere. Below ~100–700 mbar, both planets have a cool equator with peak meridional contrasts ~2-10 K (see Fig. 2 of Simon-Miller et al., 2006 and Fig. 2 of Fletcher et al., 2010). Zonal wind speeds of Jupiter's deep troposphere were extracted from the Doppler Wind Experiment at 6°N and show an increase in the velocity with depth below 1 bar (Atkinson et al., 1998). This is consistent with a positive latitudinal temperature gradient (i.e. cool equator) since the wind shear is negative. Numerical simulations of off-equatorial jets in Jupiter's and Saturn's upper atmosphere reproduce similar results (Fig. 1 of Liu and Schneider, 2015). However, wind shear near 5-micron hotspots is likely to be complex, because dynamics are affected by a planetary-scale wave in addition to zonal-mean gradients (Showman and Dowling, 2000). Neptune's measured tropospheric temperatures are the opposite to that described on Jupiter and Saturn (i.e., a warm equator instead), but this work could hint at a cool 'Jupiter-like' equator at depths >1 bar provided a flatter methane distribution. More precise constraints on Neptune's methane profile and extent of zonal flow are needed to determine if Neptune's temperature field is similar to the other jovian planets. Considering the energetics of flow in future models will also be important for relating Neptune's zonal winds, temperature field, and composition.

5.2. Global circulation

Multi-wavelength observations have been crucial for determining Neptune's global circulation pattern. de Pater et al. (2014) analyzed near-infrared cloud activity, temperature patterns, ortho/para H_2 ratios, and measurements of mid-infrared and radio temperature brightness to construct a hemispherically symmetric circulation pattern where air rises above the mid-latitudes and sinks at the equator and poles. Their single-layer circulation is broadly

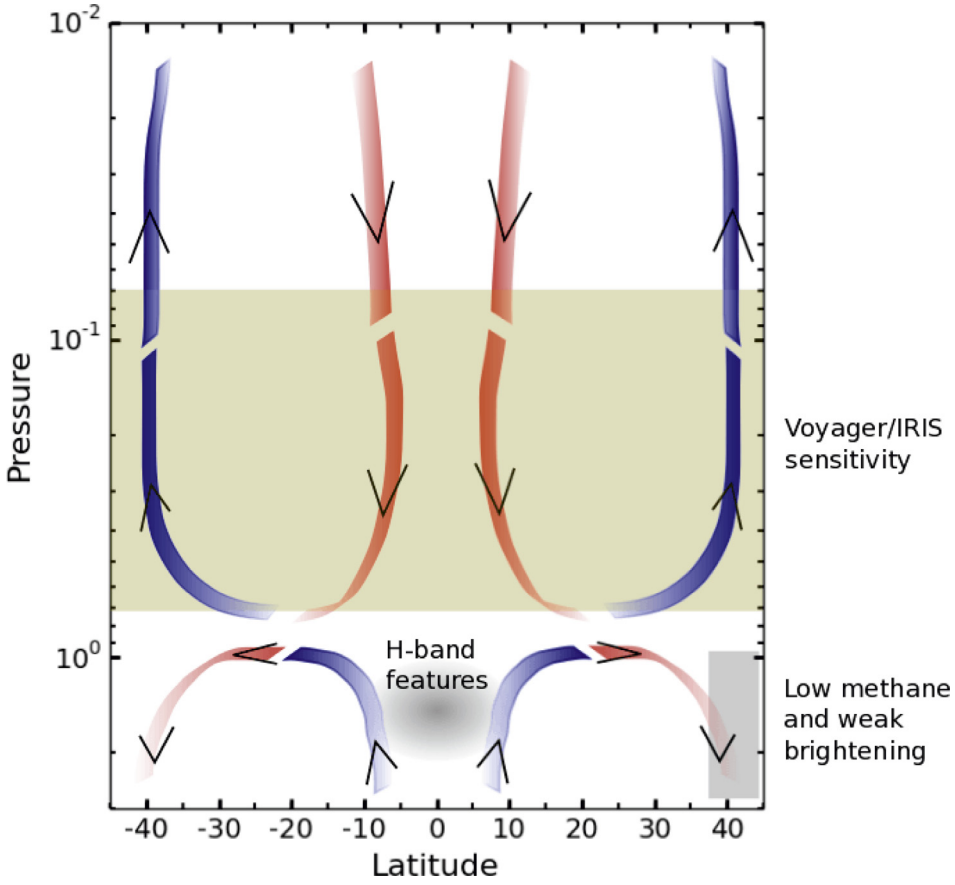

Fig. 23. Schematic of our proposed circulation model between 10 mbar and 3 bar from the equator to mid-latitudes. The colored bands and arrows indicate the direction of circulation, blue indicating cool, rising air, and red warm, sinking air. Each cell forms a closed loop, continuing outside the range shown in the figure. The depth of circulation below 1 bar is unknown. The yellow band highlights the range of Voyager/IRIS sensitivity. The equatorial clouds seen in the H-band but not the K'-band are indicated as a gray circle. The mid-latitude region of methane depletion and weak brightening from Karkoschka and Tomasko (2011) and Butler et al. (2012) is represented by a gray rectangle. (For interpretation of the references to color in this figure legend, the reader is referred to the web version of this article.)

extended, ranging from the stratosphere down to ~40 bar, and could explain most, though not all, observations at wavelengths spanning a range from the visible to 6 cm. If methane abundances are uniform or weakly varying, our data are indicative of a more complicated circulation between the equator and mid-latitudes. Below 1 bar, an equator colder than the mid-latitudes is needed to produce the predicted vertical wind shear. This scenario is consistent with air rising and cooling as it adiabatically expands at the equator while air subsides and warms due to adiabatic compression at the mid-latitudes. Such a circulation pattern is consistent with data that do not agree with the single-cell circulation in de Pater et al. (2014). Butler et al. (2012) constructed 1-cm radio maps of Neptune from data obtained with the Expanded Very Large Array (EVLA) and found weak brightness enhancements at the southern mid-latitudes, as well as strong enhancements over the pole and equator. Karkoschka and Tomasko (2011) found evidence of methane depletion between 1.2 and 3.3 bar at mid-latitudes in data acquired by the Hubble STIS spectrograph. Regions of low methane abundance and opacity indicate downwelling. Conversely, high abundances and opacities suggest upwelling. Moreover, methane-rich air will cool and condense as it rises at the equator. This may explain the presence of deep-seated H-band features. An example two-celled model that is consistent with these observations is given in Fig. 23. This modifies the model given by de Pater et al. (2014) below 1 bar to an unknown depth. A three-cell circulation pattern has been proposed for Uranus to explain polar methane depletion and cloud activity at the mid-latitudes (Sromovsky et al., 2014). Stacked circulation cells above and below the clouds of Saturn may explain spatial distributions of chemical tracers measured by Cassini/VIMS (Fletcher et al., 2011). Neptune's atmosphere may be similarly complex.

On the other hand, if methane abundances vary significantly, a warm equator can still reproduce our observed vertical wind shear. Such a temperature profile would be consistent with both: (1) the single-cell circulation model suggested by de Pater et al. (2014), and (2) direct measurements of the temperature field. Although the (de Pater et al., 2014) model explained a broad range of observations, observed variations in methane abundance are not explained by this circulation model. It is likely that an elaborate circulation model is needed to explain all known observations of Neptune's upper atmosphere. Neptune's circulation pattern may contain finer latitudinal and vertical structure than we can determine from currently available data.

6. Conclusions

We tracked the longitude-latitude positions of dozens of bright features in Neptune's atmosphere from Keck AO images on July 3, 2013 and August 20, 2014 in the H- and K'-bands. From their positions and length of time tracked, we derived zonal and meridional velocities and constructed zonal wind profiles for each band and night.

Our main conclusions are:

(1) The motions of many individually tracked cloud features are significantly different than the zonal wind speeds predicted by the canonical profile from Sromovsky et al. (1993). This dispersion is

most prominent from the equator to mid-latitudes, reaching as high as 500–600 m/s, and is seen on both nights. A few features have meridional velocities as large as 100–200 m/s. These features also tend to have the largest zonal velocity deviations from the canonical profile, suggesting they are driven by mechanisms like vortices or wave phenomena as these produce motion in both directions. Generally, features with the largest velocity variations (in both directions) have large RMS errors and are tracked for a short time. These features are usually ephemeral, faint, or near the planetary limb, meaning their centers are hard to constrain. Velocity variations also persist in low-error, long-tracked features, although the magnitude of variability is muted.

(2) There are significant differences in the zonal wind profiles between the H-band and K'-band on both nights. This is most prominent at the equator, where the H profile is best described by a profile shifted eastward by 90 ± 45 m/s on July 3, 2013 and 141 ± 63 m/s on August 20, 2014. There is little difference between the K'-band zonal wind profiles and the canonical profile. 2013 H band features have smaller Kp/H I/F ratios at the equator than the mid-latitudes. The exquisite quality of our July 3, 2013 images reveal numerous equatorial features in the H-band that are not present in K'-band. This suggests those features are located below 1 bar. Taken all together, this is consistent with the idea that the mean eastward velocity shifts in the H profile are driven by deep-seated features. Differences in velocity with depth are evidence of vertical wind shear.

(3) If the shift in the H profile is real and indicative of vertical wind shear, we predict shears between -1.0 and -2.2 m/(s km) at the equator, assuming H and K' features typically differ in altitude by 3–5 scale heights. Previous studies have dismissed vertical wind shear as an explanation for the variability between the H-band and canonical profile, claiming that thermal winds would decay (be less negative) with increasing altitude and produce the opposite of what is observed. However, this analysis relied on Voyager/IRIS temperature retrievals that are only sensitive between 70–800 mbar, outside the pressures we expect the H-band to see at the equator. Using a formulation that extends the thermal wind equation to the equator (Marcus et al., 2018), we derived the meridional temperature profiles that are needed below 1 bar to match our predicted vertical wind shear. Neglecting density effects due to variation in methane concentration, we find that the equator must be colder than the midlatitudes by 5–15 K to explain the observations, although this range can be lowered if wind shear is not uniform throughout the atmosphere. This is similar to tropospheric temperature profiles derived from mid-infrared observations and numerical simulations of Jupiter' and Saturn's atmosphere. Colder temperatures at the equator are consistent with upwelling and are not consistent with the (de Pater et al., 2014) single-layer model's equatorial downwelling.

(4) We used the generalized thermal-compositional wind equation (Sun et al., 1991) to account for density variations that result from latitudinally fluctuating methane abundances. We used this equation to re-derive the temperature structure below 1 bar needed to match expected methane variations and vertical wind shear. If methane is weakly-depleted at the mid-latitudes ($2\times$ depletion), an equator 2–3 K colder than the mid-latitudes is consistent with our inferred wind shear. This could be explained by adiabatic cooling and methane enrichment at the equator due to upwelling, but it is inconsistent with the de Pater et al. (2014) single-layer circulation with equatorial downwelling. If methane is strongly depleted at mid-latitudes ($4\times$ depletion), an equator 2–3 K warmer than the mid-latitudes is consistent with our inferred wind shear. Equatorial warming combined with methane enrichment is not consistent with either the single-layer de Pater et al. (2014) model, or the double-layer model in Fig. 23. It is, however, consistent with observed measurements of Neptune's temperature field. We emphasize the importance of including these density variations future models, as condensation regions or phase changes result in large density changes.

(5) Our results suggest a global circulation pattern more complicated than the single-celled, vertically broad model described by de Pater et al. (2014). Stacked circulation cells may explain observed methane variations and our derived temperature profiles. However, we cannot reconcile all observations of Neptune's upper atmosphere with this model. Latitudinally and vertically complex circulation cells may be needed to explain the dynamics of Neptune's atmosphere.

Multi-wavelength observations of Neptune are required to fully understand the degree of vertical wind shear and true circulation pattern in the troposphere. Cloud tracking with spectral information would verify whether features with different speeds are in fact at different depths. Radio wavelengths are sensitive to H_2S variations in Neptune's atmosphere below 1 bar. Longitudinally-resolved radio maps of Jupiter have recently been produced with the upgraded VLA (de Pater et al., 2016). Similar maps of Neptune's deep atmosphere would trace variations in the H_2S abundance and determine regions of sinking (low H_2S) and rising (high H_2S) air. This would provide a check for the stacked-celled circulation hypothesis.

Acknowledgments

The data presented were obtained at the W.M. Keck Observatory, which is operated as a scientific partnership among the California Institute of Technology, the University of California and the National Aeronautics and Space Administration. The Observatory was made possible by the generous financial support of the W.M. Keck Foundation. This work has been supported in part by the National Science Foundation, NSF Grant AST-0908575 and AST-1615004 to UC Berkeley and by NASA Headquarters: under the NASA Earth and Space Science Fellowship program Grant NNX16AP12H to UC Berkeley, and Grant NNX23AG56G under NASA Planetary Atmospheres to UC Berkeley. LNF was supported by a Royal Society Research Fellowship and European Research Council Consolidator Grant (under the European Union's Horizon 2020 research and innovation programme, grant agreement No. 723890) at the University of Leicester. The authors wish to recognize and acknowledge the very significant cultural role and reverence that the summit of Mauna Kea has always had within the indigenous Hawaiian community. We are most fortunate to conduct observations from this mountain.

Appendix A

In this appendix, we show an alternate model for the vertical wind shear: $\partial u/\partial r$ used in Section 5.1.1, Eq. (35). We assume that the vertical shear can be expanded in even 4th-order Legendre polynomials:

$$\frac{\partial u}{\partial r} = p_0 + p_1 \frac{1}{2}(3\mu^2 - 1) + p_2 \frac{1}{8}(35\mu^4 - 30\mu^2 + 3), \tag{36}$$

where $\mu = \sin\theta$. Legendre polynomials may be preferred to the 4th-order polynomials used in Section 5.1.1 since the former are solutions to Laplace's equation on the sphere and are valid expansions at the poles. Now solve for the temperature profile:

$$\log\left(\frac{T(\theta, P)}{T_0(P)}\right) = -\frac{2\Omega r_0}{g}\int_{\theta_0}^{\theta} \sin\theta' \frac{du(\theta', P)}{dr} d\theta' \tag{37}$$

$$= -\frac{2\Omega r_0}{g}\int_{\theta_0}^{\theta} \sin\theta' \left(p_0 + p_1 \frac{1}{2}(3\mu^2 - 1) + p_2 \frac{1}{8}(35\mu^4 - 30\mu^2 + 3)\right) d\theta' \tag{38}$$

The integral on the right-hand side of can be solved analytically via repeated integration-by-parts. The final solution, written for brevity, is:

$$\log\left(\frac{T(\theta,P)}{T_0(P)}\right) = -\frac{2\Omega r_0}{g}(p_0\cdot t_0 + p_1\cdot t_1 + p_2\cdot t_2) \tag{39}$$

$$T(\theta,P) = T_0(P)\cdot\exp\left[-\frac{2\Omega r_0}{g}(p_0\cdot t_0 + p_1\cdot t_1 + p_2\cdot, t_2)\right] \tag{40}$$

where:

$$t_0 = -\cos\theta$$

$$t_1 = \frac{1}{8}(\cos(3\theta) - 5\cos\theta)$$

$$t_2 = \frac{1}{384}(-21\cos(5\theta) + 55\cos(3\theta) - 114\cos\theta)$$

As before, this result be easily extended to the equator. In the following table, we compare the latitudes of the local maximal/minimal temperatures using this model and the model given in Section 5.1.1; we assume, for sake of example, an equatorial temperature of 80 K.

Section 5.1.1 model	Appendix model
0°–80.0 K	0°–80 K
38.3°–85.9 K	33.5°–84.4 K
78.2°–72.2 K	70.5°–76.0 K

The qualitative analysis is the same between these models – the equator is colder than the mid-latitudes. The peak mid-latitude temperatures differ by 1.5 K. While the model in Section 5.1.1 has a more extreme temperature change and is probably less accurate at high-latitudes, we do not consider this region in our analysis of Neptune's tropospheric temperature profiles since the zonal wind profile is wildly uncertain there - very few features are tracked in this region. Thus, the model presented in Section 5.1.1 is good enough as a base analysis - future work may explore better methods to model vertical wind shear on Neptune. We point out that analogous calculations can be used in the model presented in Section 5.1.2.

Supplementary material

Supplementary material associated with this article can be found, in the online version, at 10.1016/j.icarus.2018.04.009.

References

Andrews, D.G., Holton, J.R., Leovy, C.B., 1987. Middle Atmosphere Dynamics. Academic Press.

Atkinson, D.H., Pollack, J.B., Seiff, A., 1998. The galileo probe doppler wind experiment: measurement of the deep zonal winds on jupiter. J. Geophys. Res. Planets 103 (E10), 22911–22928. doi:10.1029/98JE00060.

Butler, B.J., Hofstadter, M., Gurwell, M., Orton, G., Norwood, J., 2012. The deep atmosphere of neptune from EVLA observations. In: Proceedings of the AAS/Division for Planetary Sciences Meeting Abstracts. In: AAS/Division for Planetary Sciences Meeting Abstracts, 44, p. 504.06.

Conrath, B.J., Gierasch, P.J., Ustinov, E.A., 1998. Thermal structure and para hydrogen fraction on the outer planets from voyager IRIS measurements. Icarus 135, 501–517.

Conrath, B.J., Flasar, F.M., Gierasch, P.J., 1991. Thermal structure and dynamics of Neptune's atmosphere from voyager measurements. J. Geophys. Res. Space Phys. 96 (S01), 18931–18939. doi:10.1029/91JA01859.

Elias, J.H., Frogel, J.A., Matthews, K., Neugebauer, G., 1982. Infrared standard stars. Astron. J. 87, 1029–1034. doi:10.1086/113185.

Fitzpatrick, P.J., de Pater, I., Luszcz-Cook, S., Wong, M.H., Hammel, H.B., 2014. Dispersion in Neptune's zonal wind velocities from NIR keck AO observations in July 2009. Astrophys. Space Sci. 350 (1), 65–88. doi:10.1007/s10509-013-1737-2.

Fletcher, L.N., Achterberg, R.K., Greathouse, T.K., Orton, G.S., Conrath, B.J., Simon-Miller, A.A., Teanby, N., Guerlet, S., Irwin, P.G., Flasar, F., 2010. Seasonal change on saturn from CASSINI/CIRS observations, 2004–2009. Icarus 208 (1), 337–352. doi:10.1016/j.icarus.2010.01.022.

Fletcher, L.N., Barnes, K., Momary, T.W., Showman, A., Irwin, P., Orton, G.S., Roos-Serote, M., Merlet, C., 2011. Saturn's tropospheric composition and clouds from CASSINI/VIMS 4.6?5.1 μm nightside spectroscopy. Icarus 214, 510–533.

Fletcher, L.N., de Pater, I., Orton, G.S., Hammel, H.B., Sitko, M.L., Irwin, P.G., 2014. Neptune at summer solstice: zonal mean temperatures from ground-based observations, 2003–2007. Icarus 231, 146–167. doi:10.1016/j.icarus.2013.11.035.

Fry, P.M., Sromovsky, L.A., 2004. Keck 2 AO observations of neptune in 2003 and 2004. Bull. Am. Astron. Soc. 1103.

Fry, P.M., Sromovsky, L.A., de Pater, I., Hammel, H.B., Rages, K.A., 2012. Detection and tracking of subtle cloud features on uranus. Astron. J. 143 (6), 150–161.

Gibbard, S.G., de Pater, I., Roe, H.G., Martin, S., Macintosh, B.A., Max, C.E., 2003. The altitude of neptune cloud features from high-spatial-resolution near-infrared spectra. Icarus 166 (2), 359–374. doi:10.1016/j.icarus.2003.07.006.

Hammel, H.B., Baines, K.H., Bergstralh, J.T., 1989. Vertical aerosol structure of neptune: constraints from center-to-limb profiles. Icarus 80 (2), 416–438. doi:10.1016/0019-1035(89)90149-8.

Hammel, H.B., Lockwood, G.W., 1997. Atmospheric structure of neptune in 1994, 1995, and 1996: HST imaging at multiple wavelengths. Icarus 129, 466–481. doi:10.1006/icar.1997.5764.

Hammel, H.B., Lockwood, G.W., 2007. Suggestive correlations between the brightness of neptune, solar variability, and Earth's temperature. Geophys. Res. Lett. 34 (8), L08203. doi:10.1029/2006GL028764.

Irwin, P.G.J., Fletcher, L.N., Tice, D., Owen, S.J., Orton, G.S., Teanby, N.A., Davis, G.R., 2016. Time variability of neptune?s horizontal and vertical cloud structure revealed by VLT/SINFONI and gemini/NIFS from 2009 to 2013. Icarus 271, 418–437.

Irwin, P.G.J., Teanby, N.A., Davis, G.R., Fletcher, L.N., Orton, G.S., Tice, D., Hurley, J., Calcutt, S.B., 2011. Multispectral imaging observations of Neptune's cloud structure with gemini-North. Icarus 216 (1), 141–158. doi:10.1016/j.icarus.2011.08.005.

Karkoschka, E., Tomasko, M.G., 2011. The haze and methane distributions on neptune from hststis spectroscopy. Icarus 211 (1), 780–797. doi:10.1016/j.icarus.2010.08.013.

Limaye, S.S., Sromovsky, L.A., 1991. Winds of neptune: voyager observations of cloud motions. J. Geophys. Res. Space Phys. 96 (S01), 18941–18960. doi:10.1029/91JA01701.

Lindal, G.F., 1992. The atmosphere of neptune – an analysis of radio occultation data acquired with voyager 2. Astron. J. 103, 967–982. doi:10.1086/116119.

Liu, J., Schneider, T., 2015. Scaling of off-Equatorial jets in giant planet atmospheres. J. Atmos. Sci. 72 (1), 389–408. doi:10.1175/JAS-D-13-0391.1.

Luszcz-Cook, S., 2012. Millimeter and near-infrared observations of Neptune's atmospheric dynamics. Thesis. University of California, Berkeley.

Luszcz-Cook, S., de Kleer, K., de Pater, I., Adamkovics, M., Hammel, H., 2016. Retrieving Neptune's aerosol properties from keck {OSIRIS} observations. I. dark regions. Icarus 276, 52–87.

Luszcz-Cook, S., de Pater, I., Ádámkovics, M., Hammel, H., 2010. Seeing double at Neptune's south pole. Icarus 208 (2), 938–944. doi:10.1016/j.icarus.2010.03.007.

Luszcz-Cook, S., de Pater, I., Wright, M., 2013. Spatially-resolved millimeter-wavelength maps of neptune. Icarus 226 (1), 437–454. doi:10.1016/j.icarus.2013.05.019.

Marcus, P.S., Tollefson, J., de Pater, I., Wong, M.H., 2018. An equatorial thermal wind equation: applications to jupiter. Icarus Submitted.

Martin, S.C., de Pater, I., Marcus, P., 2012. Neptunes zonal winds from near-IR keck adaptive optics imaging in august 2001. Astrophys. Space Sci. 337 (1), 65–78. doi:10.1007/s10509-011-0847-y.

Max, C.E., Macintosh, B.A., Gibbard, S.G., Gavel, D.T., Roe, H.G., de Pater, I., Ghez, A.M., Acton, D.S., Lai, O., Stomski, P., Wizinowich, P.L., 2003. Cloud structures on neptune observed with keck telescope adaptive optics. Astron. J. 125 (1), 364.

Moses, J.I., Fouchet, T., Bzard, B., Gladstone, G.R., Lellouch, E., Feuchtgruber, H., 2005. Photochemistry and diffusion in Jupiter's stratosphere: constraints from ISO observations and comparisons with other giant planets. J. Geophys. Res. Planets 110 (E8), E08001. doi:10.1029/2005JE002411.

de Pater, I., Fletcher, L.N., Luszcz-Cook, S., DeBoer, D., Butler, B., Hammel, H.B., Sitko, M.L., Orton, G., Marcus, P.S., 2014. Neptune'S global circulation deduced from multi-wavelength observations. Icarus 237, 211–238. doi:10.1016/j.icarus.2014.02.030.

de Pater, I., Gibbard, S.G., Hammel, H., 2006. Evolution of the dusty rings of uranus. Icarus 180 (1), 186–200. doi:10.1016/j.icarus.2005.08.011.

de Pater, I., Sault, R.J., Butler, B., DeBoer, D., Wong, M.H., 2016. Peering through Jupiter's clouds with the very large array. Science 352, 1198–1201. doi:10.1126/science.aaf2210.

Pedlosky, J., 1987. Geophysical Fluid Dynsmics. Springer-Verlag New York.

Showman, A., Dowling, T., 2000. Nonlinear simulations of Jupiter's 5-Micron hot spots. Science 289, 1737–1740.

Simon, A.A., Rowe, J.F., Gaulme, P., Hammel, H.B., Casewell, S.L., Fortney, J.J., Gizis, J.E., Lissauer, J.J., Morales-Juberias, R., Orton, G.S., Wong, M.H., Marley, M.S., 2016. Neptune'S dynamic atmosphere from kepler K2 observations: implications for brown dwarf light curve analyses. Astrophys. J. 817 (2), 162–171.

Simon-Miller, A.A., Conrath, B.J., Gierasch, P.J., Orton, G.S., Achterberg, R.K., Flasar, F.M., Fisher, B.M., 2006. Jupiter'S atmospheric temperatures: from voyager IRIS to cassini CIRS. Icarus 180 (1), 98–112. doi:10.1016/j.icarus.2005.07.019.

Smith, B.A., Soderblom, L.A., Banfield, D., Barnet, c., Basilevsky, A.T., Beebe, R.F., Bollinger, K., Boyce, J.M., Brahic, A., Briggs, G.A., Brown, R.H., Chyba, c., Collins, s.A., Colvin, T., Cook, A.F., Crisp, D., Croft, S.K., Cruikshank, D., Cuzzi, J.N., Danielson, G.E., Davies, M.E., De Jong, E., Dones, L., Godfrey, D., Goguen, J., Gre-

nier, I., Haemmerle, V.R., Hammel, H., Hansen, c.J., Helfenstein, c.P., Howell, C., Hunt, G.E., Ingersoll, A.P., Johnson, T.V., Kargel, J., Kirk, R., Kuehn, D.I., Limaye, S., Masursky, H., McEwen, A., Morrison, D., Owen, T., Owen, W., Pollack, J.B., Porco, c.c., Rages, K., Rogers, P., Rudy, D., Sagan, C., Schwartz, J., Shoemaker, E.M., Showalter, M., Sicardy, B., Simonelli, D., Spencer, J., Sromovsky, L.A., Stoker, C., Strom, R.G., Suomi, V.E., Synott, S.P., Terrile, R.J., Thomas, P., Thompson, W.R., Verbiscer, A., Veverka, J., 1989. Voyager 2 at neptune: imaging science results. Science 246 (4936), 1422–1449. http://www.sciencemag.org/content/246/4936/1422.full.pdf

Sromovsky, L.A., Fry, P.M., Hammel, H.B., Ahue, W.M., de Pater, I., Rages, K.A., Showalter, M.R., van Dam, M.A., 2009. Uranus at equinox: cloud morphology and dynamics. Icarus 203 (1), 265–286. doi:10.1016/j.icarus.2009.04.015.

Sromovsky, L.A., Fry, P.M., 2005. Dynamics of cloud features on uranus. Icarus 179 (2), 459–484.

Sromovsky, L.A., Fry, P.M., Baines, K.H., Limaye, S.S., Orton, G.S., Dowling, T.E., 2001a. Coordinated 1996 HST and IRTF imaging of neptune and triton: i. observations, navigation, and differential deconvolution. Icarus 149 (2), 416–434. doi:10.1006/icar.2000.6562.

Sromovsky, L.A., Fry, P.M., Dowling, T.E., Baines, K.H., Limaye, S.S., 2001b. Coordinated 1996 HST and IRTF imaging of neptune and triton: III. Neptune's atmospheric circulation and cloud structure. Icarus 149 (2), 459–488. doi:10.1006/icar.2000.6564.

Sromovsky, L.A., Fry, P.M., Dowling, T.E., Baines, K.H., Limaye, S.S., 2001c. Neptune'S atmospheric circulation and cloud morphology: changes revealed by 1998 HST imaging. Icarus 150, 244–260. doi:10.1006/icar.2000.6574.

Sromovsky, L.A., Fry, P.M., Hammel, H.B., de Pater, I., Rages, K.A., 2012. Post-equinox dynamics and polar cloud structure on uranus. Icarus 220 (2), 694–712. doi:10.1016/j.icarus.2012.05.029.

Sromovsky, L.A., Fry, P.M., Limaye, S.S., Baines, K.H., 2003. The nature of Neptune's increasing brightness: evidence for a seasonal response. Icarus 163 (1), 256–261. doi:10.1016/S0019-1035(03)00069-1.

Sromovsky, L.A., Karkoschka, E., Fry, P.M., Hammel, H.B., de Pater, I., Rages, K., 2014. Methane depletion in both polar regions of uranus inferred from HST/STIS and keck/NIRC2 observations. Icarus 238, 137–155. doi:10.1016/j.icarus.2014.05.016.

Sromovsky, L.A., Limaye, S.S., Fry, P.M., 1993. Dynamics of Neptune's major cloud features. Icarus 105 (1), 110–141. doi:10.1006/icar.1993.1114.

Sun, Z.-P., Stoker, C.R., Schubert, G., 1991. Thermal and humidity winds in outer planet atmospheres. Icarus 91 (1), 154–160.